DNA origami-based platform for multi-axial single-molecule force spectroscopy reveals hidden dynamics in Holliday junctions

Gde Bimananda Mahardika Wisna[a,c,d], **Ayush Saurabh**[a,d], **Ranjan Sasmal**[c], **Deepak Karna**[c], **Prathamesh Chopade**[c], **Steve Pressé**[a,b,d], **and Rizal F. Hariadi**[a,c,d,1]

[a]Department of Physics, Arizona State University, Tempe, Arizona, USA.; [b]School of Molecular Sciences, Arizona State University, Tempe, Arizona, USA.; [c]Center for Molecular Design and Biomimetics at the Biodesign Institute, Arizona State University, Tempe, Arizona, USA.; [d]Center for Biological Physics, Arizona State University, Tempe, Arizona, USA.

[1]To whom correspondence should be addressed. E-mail: rhariadi@asu.edu

This manuscript was compiled on June 10, 2025

Abstract

In living cells, biomolecules operate in a crowded 3D milieu and are subjected to complex multi-axial stress environment. These mechanical forces are fundamental regulators of biomolecular structures and functions. However, most single-molecule force spectroscopy techniques primarily exert force along a single axis, thereby failing to recreate the mechanical environments experienced by biomolecules in cells. Here, we present a molecular tool comprising a multi-axial entropic spring tweezer along rigid DNA origami (MAESTRO), which utilizes ssDNA entropic springs to apply forces in the piconewton (pN) range and is designed to examine the dynamics of biomolecules under defined multi-axial tensions. Combining MAESTRO, single-molecule Förster resonance energy transfer (smFRET) and Bayesian non-parametric FRET (BNP-FRET) enables high-throughput study of biomolecules under different complexities of multi-axial tension forces. We demonstrate our tension-inducing molecular tool on Holliday junction (HJs)—intermediate DNA structures important in the homologous recombination process. Instead of faster kinetics under tension, we discovered $\geq 5\times$ slower kinetics of the HJ conformations under multi-axial tension than under tension-free conditions, which in turn permits direct observations of intermediate open and unstacked HJ conformations. Notably, under four-way tension, we observed clear evidence of inter-conversion between several different kinetic patterns in many individual HJs, previously believed to be non-interconverting owing to the rugged energy landscape of the system. In addition to controlling conformational dynamics, we show that the tension experienced by HJ also mechanically tunes the functional outcome of T7 endonuclease I, a junction-resolving enzyme that recognizes HJ and catalyzes two cleavage sites within the junction. By overcoming the limitations of single-axial force spectroscopy, we envision that MAESTRO's versatile multi-axial tension capability will enable high-throughput investigation of complex, previously unseen dynamics and probe the mechanoregulation of many biomolecules.

Key words: single-molecule dynamics, DNA origami, force spectroscopy, multi-axial tension, single-molecule FRET, Holliday junction

Introduction

Mechanical forces on the order of piconewton (pN) acting at the single-molecule level have a profound effect on biomolecular function by inducing nanometer-scale structural changes. The mechanisms that give rise to mechanical forces can be either active, where a molecule converts chemical energy into mechanical work, or passive, as it experiences pulling and stretching from surrounding biomolecules. The strengths of this mechanical work are comparable to the thermal energy scale of $k_BT \sim 4.2$ pN.nm, suggesting that multi-axial tension forces broadly influence biomolecular processes.[1]

To investigate the mechanics at the single-molecule level, a variety of revolutionay force spectroscopy tools have been utilized, including optical[2] and magnetic tweezers[3], atomic force microscopy[4], centrifugal force spectroscopy[5], DNA-based tension probes[6–9], and a DNA nanoscopic force clamp[10,11], often in tandem with single-molecule fluorescence microscopy[12]. These approaches have successfully quantified the mechanical energy generated by the rotary motor F1-ATPase under specified loads[13], identified the stall force of motor proteins such as myosins and kinesins[14,15], measured the stalling tension in T7-DNA polymerase[16], investigated stacking forces among DNA bases[17], observed conformational changes of DNA Holliday junctions under tension[18], analyzed the activation of different mechanosensitive membrane proteins[6–9], and explored the energetics involved in protein folding and unfolding.[19,20] These techniques efficiently address numerous aspects of single-molecule biophysics, achieving high precision over a diverse range of tensions, as seen with atomic force microscopy and magnetic tweezers, and providing high-throughput capabilities, as demonstrated by magnetic tweezers, centrifugal force spectroscopy, DNA origami-based spectroscopy, and DNA-based tension probes. However, they are limited to applying tension forces in a single direction due to challenges related to alignment and stability, the complexity of force calibration and measurement, and the difficulties in incorporating multiple tether or anchor points without inducing twisting or buckling.[21–23]

Yet, in biologically relevant scenarios, many biomolecules experience tension along multiple directions due to complex intermolecular interactions, thereby establishing multiple connections with neighboring biomolecules, such as those found in proteins involved in the focal adhesion complex.[24,25] For example, integrin, a force receptor protein that spans the cell membrane, forms connections with the extracellular matrix through its head, and with actin networks through one of its intracellular tails while the other tail is anchored in the lipid bilayer.[26,27] Despite the biological relevance, methods to exert multi-axial tension and simultaneously monitor biomolecular activity have yet to be developed.

To address this limitation, we employ DNA origami[28,29] and entropic springs[11,30] to induce tension forces along multiple directions. With DNA origami, any rigid 3D shape can be realized through the folding of a long single-stranded DNA (ssDNA) scaffold with hundreds of short ssDNA staple strands via Watson-Crick base-pairing. We choose a 3D cylindrical DNA origami as a rigid platform with circular symmetry[31] to pattern several ssDNAs with specific lengths spanning the diameter of the origami structure. These ssDNA strands act as entropic springs that can generate specific tensions in the range $0 - 12$ pN along the spring via thermal fluctuations.[11,30]

Finally, we use our multi-axial entropic spring tweezer along rigid origami (MAESTRO) to study the dynamics and conformational changes of DNA Holliday junctions (HJ) under several tension configurations using single-molecule fluorescence resonance energy transfer (smFRET). HJs appear with four DNA duplex arms joined via a four-way junction during the intermediate process of homologous recombination.[32–37] Under tension-free conditions, dynamics and conformations of different HJ sequences have been extensively studied.[11,18,38–40] HJs are known to have two conformations of isomer-I and isomer-II and undergo active switching through intermediate open conformations.[18,38,41] Additionally, HJs have been shown to have dynamical variations among identical molecules due to rugged energy landscape of the system[11,40] causing ergodicity to be broken. Physiologically relevant single-axial tension forces have been introduced to HJs as well using optical tweezers and DNA origami force-clamps to study the effects of tension on HJ dynamics and conformations. Under such tension forces, HJ transition rates and relative conformation populations are significantly affected depending on the direction of application and are very sensitive to pN scale changes in tension.[11,18] These characteristics make HJ an ideal model system for studying biomolecules under tension,

possessing a simple DNA structure yet having complex dynamical properties that can be modified by tension.

Our experiments using MAESTRO, for the first time, reveal HJ dynamics under multi-axial tension, which we find to be kinetically very heterogeneous with various combinations of fast and slow rates for both high and low FRET conformations. Specifically, we observe over 5× slower kinetics as compared to dynamics under tension-free conditions, in turn allowing to observe previously unseen, short-lived intermediate states. Moreover, our data suggests that multi-axial tension facilitates many HJ molecules to inter-convert between different kinetic patterns with their unique sets of transition rates among the conformations.

Results

HJs serve as intermediates in homologous recombination, a process likely impacted by multi-axial mechanical forces. During mitosis and meiosis, ionizing agents or malfunctioning replication machinery can damage DNA.[42–44] Homologous recombination plays a crucial role in repairing such DNA double-strand breaks (Fig. 1a(i)). This repair mechanism involves the formation of an intermediate DNA structure containing double HJs or a single HJ.[42,43] A single HJ forms through a process called D-loop nicking. Specific endonucleases mediate this step, followed by second-end capture[43] (Fig. 1a(ii)). During these events, DNA strands from homologous chromosomes undergo chromatin remodeling.[45] Such remodeling enables the homology search and gene pairing, which are essential to initiate strand invasion. These search and pairing processes require long stretches of accessible DNA.[45] Furthermore, these stretches remain connected and are more loosely wrapped around histones than in compact chromatin, which is typical when homologous recombination is inactive.

As DNA strands are still bound to histones, we hypothesize that multi-axial tension forces act on the single HJ prior to its resolution by resolvases (Fig. 1a(iii)). These tension forces could influence how the enzyme binds to HJ and bias the enzyme to cut one pair of DNA nicks over the other pair, potentially guiding the process toward either crossover or non-crossover products (Fig. 1a(iii)). Therefore, multi-axial tension could potentially influence the genetic outcome of DNA repair in cells.

MAESTRO creates a multi-axial tension environment. The architecture of MAESTRO comprises a rigid ring with a diameter of $\sim$ 45 nm and a height of $\sim$ 14 nm, constructed from 16 curved DNA helices.[31] Its circular symmetry enables the anchoring of multiple single-stranded DNA (ssDNA) entropic springs along the inner sidewalls, which apply single direction or multi-axial tension forces to the HJ (Fig. 1b, S1 and Table S1). We investigated the dynamics of HJ under various tension configurations using single-molecule Förster Resonance Energy Transfer (smFRET). A FRET pair was placed on the HJ, and smFRET trajectories were collected via a total internal reflection fluorescence (TIRF) microscope (Fig. 1b,c).

Our smFRET experiments reveal a wide range of kinetic behaviors among the HJs under tension, implying that each smFRET trajectory can have a distinct set of transition rates between the HJ conformations. Consequently, to observe previously unseen dynamics, we cannot fix the number of states in advance for the entire population when analyzing our smFRET datasets, as is commonly performed when using traditional hidden Markov model (HMM)-based techniques.[46] As such, we chose to use Bayesian non-parametric FRET (BNP-FRET)[46,47] to analyze the smFRET trajectories and extract key kinetic parameters. This method implements an infinite-dimensional HMM and uses Markov chain Monte Carlo (MCMC) techniques to generate samples for the number of states, state trajectories, transition rates, and FRET efficiencies. Furthermore, BNP-FRET uses an accurate noise model for our sCMOS camera and incorporates pixel-by-pixel camera calibration maps to best recover the signal from the noisy smFRET data. Finally, BNP-FRET samples can then be collected together to generate heat maps for escape rates λ (sum of all transition rates out of a given state) as well as transition densities (Fig. 1c and d), and estimate uncertainties.

Verification of MAESTRO structure. We employ negative-stain transmission electron microscopy (ns-TEM) to validate that MAESTRO retains its programmed rigid and circular structure (Fig. 1e, left panel).

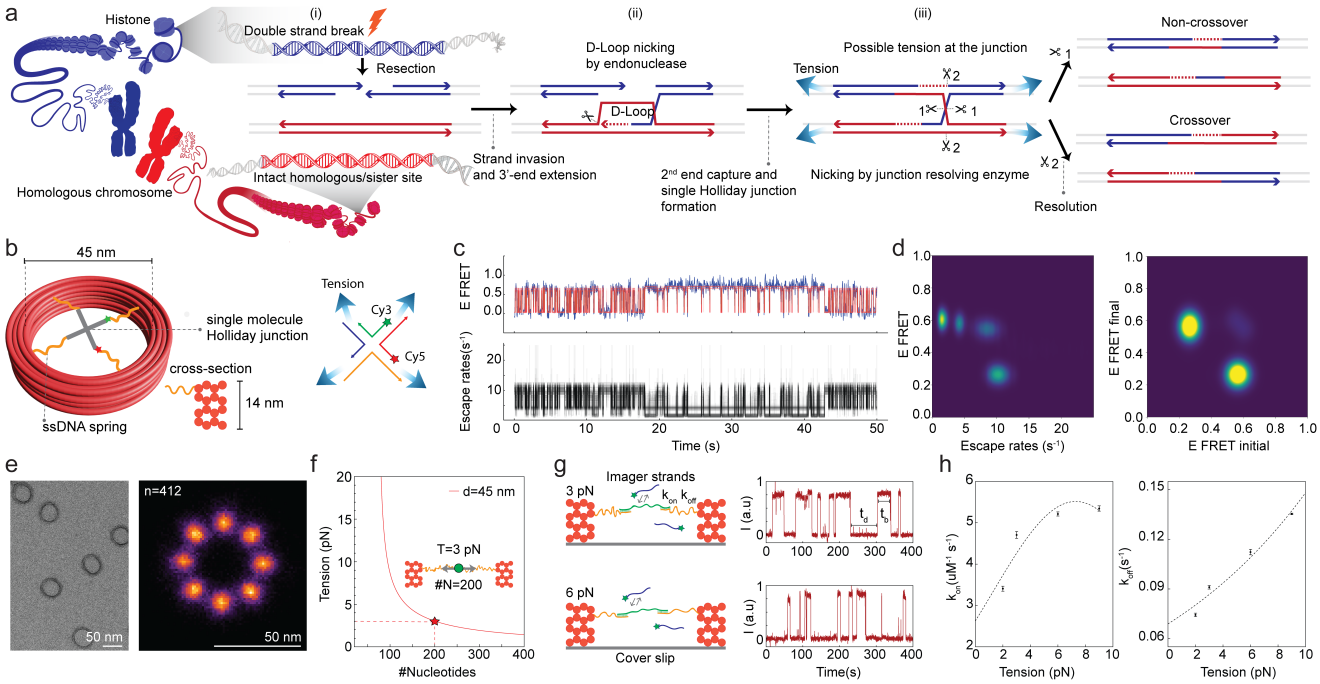

Fig. 1 HJ under multi-axial tension forces during homologous recombination, MAESTRO's design for smFRET under multi-axial tension forces, and tension forces characterization. (**a**) Homologous recombination following a double-strand break leads to the formation of a single Holliday junction (HJ) as an intermediate. This junction remains under tension forces prior to resolution due to loose histone wrapping during chromatin remodeling. (**b**) Schematic of the MAESTRO design with an HJ positioned under multi-axial tension. (**c**) Representative smFRET trajectory (blue) overlaid with MCMC samples for state trajectory (red) generated by BNP-FRET, showing HJ dynamics under multi-axial tension (top panel), along with corresponding escape rates (bottom panel). (**d**) Heatmaps for escape rates λ (left) and transition density (right) obtained from $n = 1000$ BNP-FRET samples. (**e**) ns-TEM image of MAESTRO (left panel) and averaged DNA-PAINT image of $n = 412$ molecules (right panel). (**f**) Tension-extension curve based on the modified FJC model (Eq. 1) for non-interacting ssDNA. (**g**) Schematic of ssDNA undergoing hybridization and de-hybridization under 3 and 6 pN tension force (left panel), and corresponding fluorescence intensity trajectories (right panel) showing bright (t_b) and dark time (t_d). (**h**) Plots of association rate (k_{on}) and dissociation rate (k_{off}) as functions of applied tension, along with fitted curves based on Equation 3 and Equation 4. Error bar is the standard deviation obtained by bootstrapping three times.

This rigidity is critical for reliably anchoring entropic ssDNA springs and for ensuring accurate tension force estimates based on the freely-jointed chain (FJC) model.[11,30] Additionally, we perform DNA-PAINT super-resolution imaging[48] to demonstrate the addressability of defined sites on the inner sidewall of MAESTRO. The results (Fig. 1e, right panel) show 8 specific attachment sites, where 2–8 oligonucleotides can be precisely connected to MAESTRO and meet at a target molecule at the center of MAESTRO. We calculate the required number of nucleotides in the ssDNA spring to generate a desired tension force by employing the modified FJC model (Fig. 1f), see Method section for the details of the model. For instance, achieving a force of 3 pN requires a ssDNA spring of 200 nucleotides to span the inner diameter of MAESTRO (Fig. 1f inset). By varying the number of nucleotides, we can generate different tension forces.

Tension characterization via the hybridization kinetics of 2 complementary short oligonucleotides. To validate the ability of MAESTRO to exert well-defined tension forces on target molecules, we developed a quantitative single-axis assay based on hybridization kinetics of 2 complementary short oligonucleotides. In this assay, one strand (termed the docking strand) is held under a defined tension, while the complementary strand diffuses freely in solution until hybridization occurs under tension. By monitoring how applied

tension influences both the association and dissociation rates of the oligonucleotide pair, we obtain direct and quantitative evidence that MAESTRO can generate controllable forces along the tethered docking strand.

We implement the kinetic measurement using DNA-PAINT super-resolution imaging. By varying the lengths of ssDNA springs, we generate predicted tension forces of 2, 3, 6, and 9 pN along the docking strands. We extract bright and dark dwell times from individual binding events (Fig. 1g) and fit the distributions using exponential functions to determine the association rate (k_{on}) and dissociation rate (k_{off}) (Fig. S2). Both k_{on} and k_{off} increased exponentially with the applied tension (Fig. 1h), indicating that the hybridization and de-hybridization processes proceed faster at higher forces.

The association rate k_{on} exponentially approaches a plateau at 6 pN with increasing tension. In contrast, k_{off} grows expoentially across the entire range of applied forces (see Methods for the details of fitting of the experimental data). These trends are consistent with those of previous studies on force-induced oligo dissociation,[49] confirming that MAESTRO applies precise low-range tension from 0 to 9 pN along the entropic spring. Furthermore, we obtain a fitted $k_{\text{on}}(0)$ of 2.63 $\mu\text{M}^{-1}\text{s}^{-1}$, in close agreement with the reported values for the identical imager sequence.[50]

J7 Holliday junctions can be classified into distinct dynamic groups based on escape rates, which reflects a rugged energy landscape with non-interconverting groups. We investigate the J7 Holliday junction (Table S2), shown to transition between 2 stacked isomers, Iso-I and Iso-II, through a short-lived open unstacked state[11,18,40] (Fig. 2a). To study how tension affects junction dynamics, we apply single-axial tension along the x and y axes at force levels of 0, 2, and 3 pN. To explore multi-axial tension effects, we introduce 2 configurations of 3-way tension forces (Fig. 2b and c).

Following the work by Hyeon et al.[40], where they are able to classify Holliday junction smFRET traces based on kinetics, here we use a similar empirical approach to categorize the kinetic behavior. We find that our data can be categorized into five distinct classes. Intuitively, these five classes can be distinguished based on the ratio of mean escape rates, $r = \lambda_{\text{Iso-I}}/\lambda_{\text{Iso-II}}$. We identify the mean escape rate values using k-means clustering of MCMC samples for each smFRET trace (see Fig. S3). That is, we have: extremal classes I ($r < 0.2$) and V ($r > 5.0$) where the Holliday junction gets stuck in either of the two conformations Iso-I (high FRET) or Iso-II (low FRET); class III ($0.9 < r < 1.1$) where the Holliday junction switches between the two conformations at approximately the same rate; and lastly, classes II and IV where the Holliday junction escape rates take intermediate values between the previously defined classes, as shown in Fig. 2d for the case of 0 pN tension. These classes show clear differences in their smFRET histograms and escape rate profiles (Fig. 2d). This variability likely arises from the rugged energy landscape of the junction, as previously proposed by Hyeon et al.[40], where complex interactions between Mg^{2+} ions and the junction structure create multiple kinetic traps. Consistent with their findings, our trajectories show no interconversion at 0 pN between classes within a 50 s observation window, under buffer conditions containing 12.5 mM Mg^{2+}.

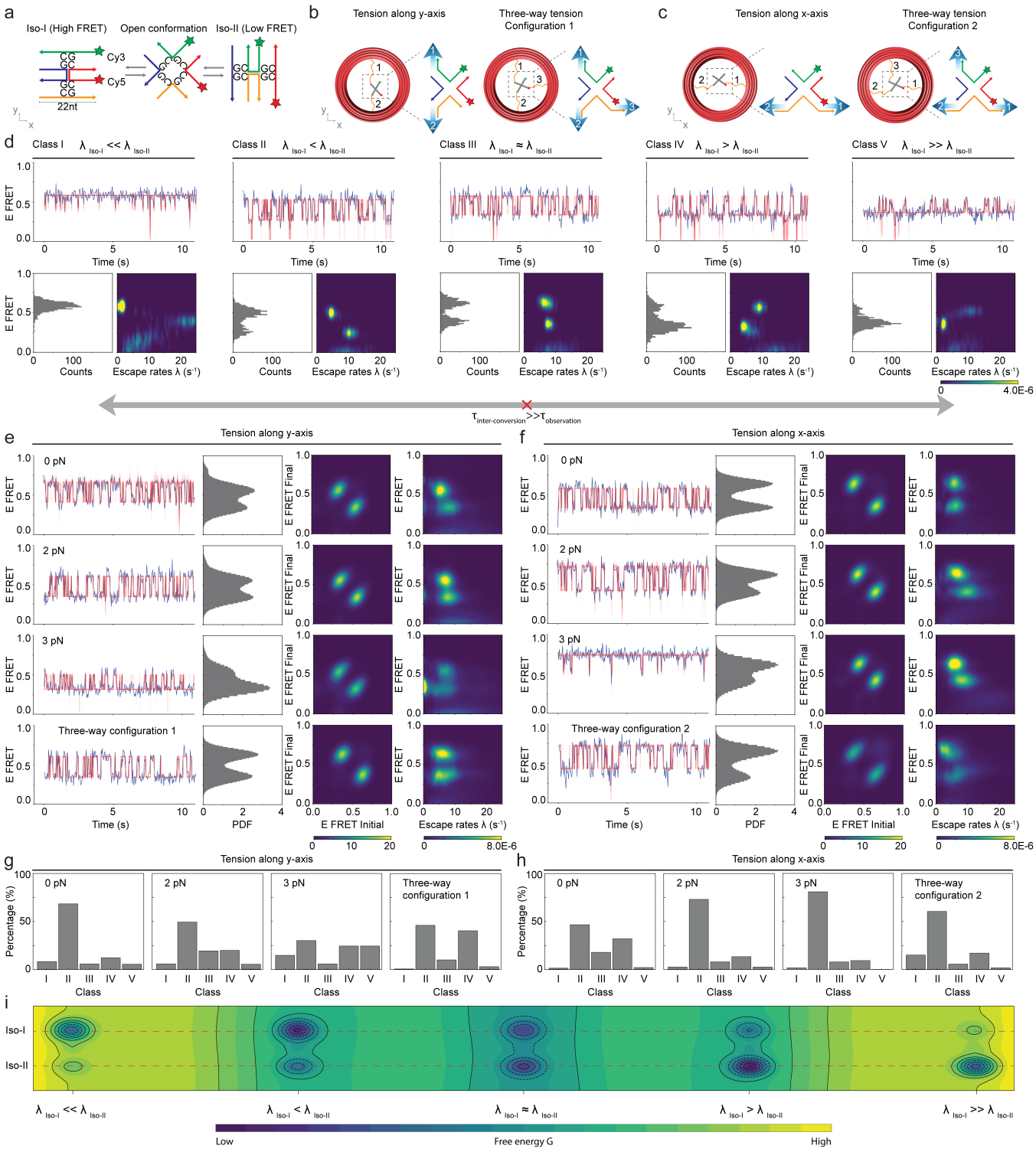

Single-axial and three-way tension forces alter J7 HJ conformation populations and escape rates, revealing opposite trends along orthogonal axes. Increasing the tension along the y-axis using spring 1 and spring 2 shifts the population toward the Iso-II state, thereby reducing the relative occupancy of Iso-I. This tension-induced population shift is clearly visible in the ensemble FRET histograms at 0, 2, and 3 pN (Fig. 2e, column 2 panels). However, introducing spring 3 to apply three-way tension forces balances the conformation populations, resulting in nearly equal occupancy of Iso-I and Iso-II (Fig. 2e, column 2, row 4).

Across all conditions, most molecules transition between two well-defined FRET states with efficiencies of

Fig. 2 (Previous page) HJs under single-axial and three-way tension forces configuration. (**a**) Schematic of the J7 Holliday junction (HJ) showing Iso-I, Iso-II, and open conformations, with a FRET pair (Cy3 and Cy5) attached to the ends of two arms. (**b, c**) Schematics illustrating how the HJ is connected to MAESTRO for different tension configurations: single-axial tension along the y and x-axes, and two configurations of three-way tension forces. Labels 1, 2, and 3 represent distinct ssDNA entropic springs. (**d**) Five classes of smFRET trajectories grouped based on the relative escape rates of the conformations. Top panels show representative smFRET (blue) and HMM (red) trajectories. Bottom panels show the corresponding smFRET histograms and escape rate heatmap. The absence of interconversion between classes suggests that $\tau_{\text{inter-conversion}} \gg \tau_{\text{observation}}$. (**e, f**) smFRET (blue) and BNP-FRET trajectories (red), ensemble smFRET histograms, transition density plots, and escape rate heatmaps compiled from $n > 150$ molecules under different tension force configurations: (e) y-axis and three-way tension forces configuration 1, (f) x-axis and three-tension forces configuration 2. (**g, h**) Histograms showing the percentage of HJ molecules classified into each of the five dynamic classes under different tension conditions: (g) y-axis and three-way tension forces configuration 1, (h) x-axis and three-way tension forces configuration 2. (**i**) Qualitative visualization of the inferred energy landscapes corresponding to the five dynamic classes.

$E \sim 0.3$ (Iso-II) and $E \sim 0.6$ (Iso-I), a hallmark of the canonical HJ behavior.[38] This dynamics is captured as two dense hotspots in the transition density heat maps (Fig. 2e, column 3). As tension along the y axis increases, the escape rate distribution shows that $\lambda_{\text{Iso-II}}$ changes to slower values, while $\lambda_{\text{Iso-I}}$ changes to faster rates (Fig. 2e, column 4, compare row 1 to row 3). Under three-way tension, however, the escape rates of both conformations become more balanced and span a wider range, in contrast to the asymmetric distribution observed at 0 pN (Fig. 2e, column 4, compare row 1 and row 4).

We observe the opposite trend when tension was applied along the x-axis (Fig. 2f). That is, increasing the force from 0 to 3 pN favors the Iso-I state over Iso-II, as shown in the ensemble FRET histograms (Fig. 2f, column 2, rows 1–3). Transitions still predominantly occur between the two main conformations (Fig. 2f, column 3), but the escape rate behavior reverses: $\lambda_{\text{Iso-I}}$ slows down while $\lambda_{\text{Iso-II}}$ increases with tension (Fig. 2f, column 4, compare row 1 to row 3).

We also note that in the case of 3pN tension along y-axis, HJ gets stuck in Iso-II, as indicated by the bright spot near 0 s^{-1} escape rate at low FRET efficiency in Fig. 2e, row 3, column 4. We also observe such behavior when the tension is along x-axis, as observed in the trace shown in Fig. 2f, row 3, column 1, albeit with far fewer molecules, as indicated by the lack of a similar bright spot at high FRET efficiency in the corresponding ensemble escape rate heatmap.

Applying three-way tension forces via spring 3 in this orientation again balances the escape rates between Iso-I and Iso-II, while broadening their overall distributions. This behavior mirrors the trend observed in the experiments along th y-axis. These findings suggest that the three-way tension enables the HJs to access a broader portion of the conformational energy landscape.

Tension redistributes HJ dynamic classes, suggesting distinct free energy levels within a rugged energy landscape. We observe clear shifts in the distribution of HJ dynamic classes as tension is applied along the y and x-axes and under three-way tension forces (Fig. 2g and h, respectively). When pulling along the y-axis, class II dominates the population at 0 pN, but the distribution progressively shifts toward higher classes (class III to class V) as the tension increases (Fig. 2g, columns 1–3). Introducing spring 3 to apply three-way tension forces (configuration 1) eliminates most of class V (Fig. 2g, columns 3 and 4), thus re-balancing the distribution.

In contrast, pulling along the x-axis at 0 pN still results in class II being the most populated, but with noticeable contributions from classes III and IV (Fig. 2h, column 1). A comparison of 0 pN results from the y and x-axis configurations (Fig. 2g vs. 2h, column 1) highlights the differences that may arise solely from the physical connection between HJ and MAESTRO. In the 0 pN setup, tension is eliminated by connecting only spring 1 while leaving spring 2 unconnected (Fig. 2b and c). This subtle difference in the anchoring of HJ to MAESTRO at 0 pN between the x and y axes alters the dynamics of HJ, affecting the relative populations of classes II, III, and IV even in the absence of external force. As tension increases along the

x-axis, the class distribution shifts leftward, favoring class II (Fig. 2h, columns 1 to 3). The application of three-way tension forces in configuration 2 also favors class II and class IV, similar to the trend observed in configuration 1 (Fig. 2h, column 4).

These results suggest that the applied tension biases the junction arms toward alignment along the force direction, thereby stabilizing one conformation over the other. This conformational preference alters both the relative population and escape rates of Iso-I and Iso-II. The observed trends agree with earlier findings from optical tweezer experiments on Holliday junctions under tension[18] and DNA origami-based force using entropic springs.[11] Together, these findings confirm that MAESTRO effectively applies mechanical tension to HJ molecules, reshaping their dynamical behavior.

We further interpret the class distributions to elucidate the relative free-energy landscape across all five classes. Combining the counts at 0 pN along x- and y-axis, classes II, III, and IV dominate, whereas classes I and V are less frequently occupied. Applying tension shifts the population toward either class I or V, depending on the direction of tension. This behavior suggests that classes I and V reside at higher free energy states compared to the intermediate classes (Fig. 2i). Although interconversion between classes remains rare within the experimental timescale under both single-axial tension and three-way tension forces, the distinct escape-rate distributions and class occupancies confirm that tension profoundly modulates the rugged conformational energy landscape of the Holliday junctions.

Four-way tension significantly slows down the transition dynamics of J7 HJ. We further explore the dynamics of J7 HJs under multi-axial tension using four-way tension forces (Fig. 3a, left and middle panels). In this setup, thermal fluctuations cause each entropic spring, attached to one of the four arms, to stochastically pull the junction in different directions (Fig. 3a, right panel).

Despite the increased mechanical complexity, the ensemble smFRET histogram still reveals a two-conformation system (Fig. 3b). Although HJs are pulled from all sides, most molecules show significantly slower transition dynamics between conformations, as illustrated by representative smFRET traces that resemble class I and class V behaviors (Fig. S4). The escape rates extracted from the the trajectories of 139 molecules exhibit a high density of values that are at least 5× slower than those observed under the 0 pN condition (Fig. 3b, middle panel; compared with Fig. 2e, 0 pN panels). These kinetics are characteristic of classes I and V, indicating a pronounced reduction in conformation switching rates.

Our data suggest that four-way tension does not prevent transitions between conformations. Instead, it significantly slow the escape rates associated with the two dominant smFRET states: $E \sim 0.3$ (Iso-II) and $E \sim 0.6$ (Iso-I). Transitions continue to occur primarily between Iso-I and Iso-II, as shown by the concentrated hotspots in the transition density plot (Fig. 3b, right panel).

We propose that mechanical tension modulates HJ conformational dynamics through a mechanism analogous to ionic effects, specifically by altering the internal multiloop topology at the crossover point. This hypothesis is supported by previous observations from McKinney et al., who demonstrated that increasing magnesium ion concentration to 50 mM resulted in comparably slow escape rates.[38] This effect occurs because divalent cations are well known to stabilize the stacked conformations of HJs and promote the formation of Iso-I and Iso-II.[51] Moreover, at high Mg^{2+} concentrations, HJs can adopt a range of secondary structures with internal multiloop topologies at the crossover point,[40] and these topologies have been shown to influence the conformational switching kinetics of HJs. Therefore, we suggest that mechanical tension functions analogously to ionic conditions, modulating the escape rates of Iso-I and Iso-II through alterations in the junction's internal multiloop topology.

Compared to single-axial tension, four-way tension forces are likely to be more effective in perturbing these internal structures in a two-dimensional space. This enhanced mechanical influence results in a higher density of slower escape rates for both conformations, contributing to a more intricate and heterogeneous dynamic HJ landscape.

Four-way tension facilitates interconversion between smFRET dynamic classes within 50 s observation period. In addition to J7 HJs remaining in a single class (class I or class V) with slow escape rates throughout

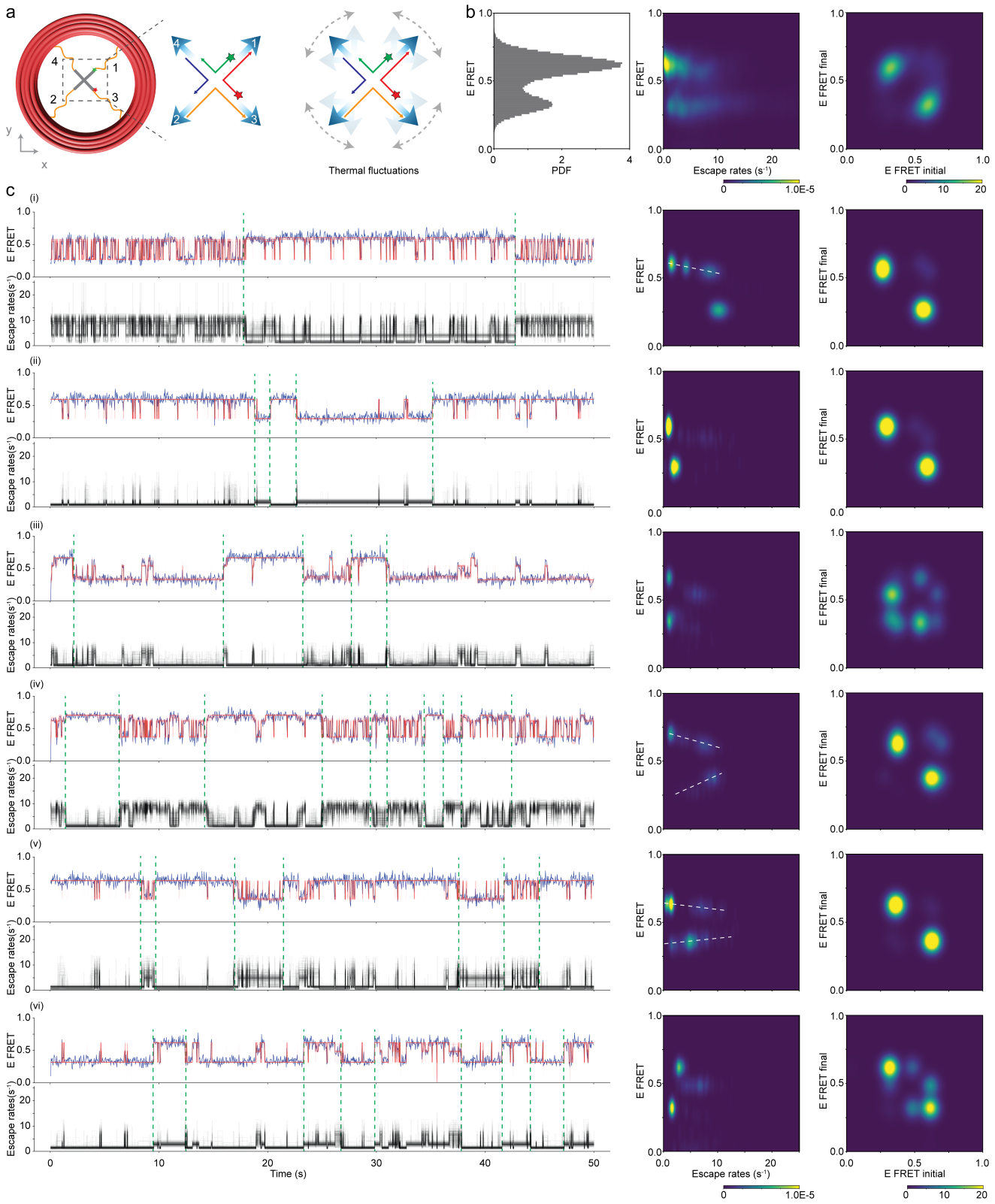

the 50 s observation window (Fig. S4), we observe many molecules undergoing clear interconversions between classes under four-way tension forces (Fig. 3c).

In the first example (Fig. 3c(i)), the molecule transitions between fast-switching conformation states (class II, III, and IV) and class I, where the junction becomes mostly trapped in the Iso-I conformation.

Fig. 3 (Previous page) Interconversion between smFRET dynamic classes in J7 HJs under multi-axial tension from four-way tension forces. (**a**) Schematic of the four-way tension configuration on a Holliday junction (HJ), showing both the structural setup (left and middle panels) and possible directions in which each entropic spring can stochastically pull the junction due to thermal fluctuations (right panel). (**b**) Ensemble smFRET histogram, escape rate distributions, and transition density heatmaps from $n = 139$ HJ molecules. (**c**) Six representative smFRET trajectories (blue) overlaid with BNP-FRET trajectories (red) (top-left panels), accompanied by their corresponding escape rate trajectories (bottom-left panels), extracted escape rates (middle panels), and transition density heatmaps (right panels). Green dashed lines indicate visually identified interconversion points between smFRET dynamic classes based on changes in escape rate behavior. White dashed lines in some heatmaps highlight subtle shifts in FRET efficiency between distinct Iso-I and Iso-II conformations.

The corresponding escape rate trajectory and heatmap reveal multiple degenerate states with escape rates of ~ 1 s^{-1}, ~ 4 s^{-1}, and ~ 9 s^{-1}, all near the same FRET efficiency ($E \sim 0.6$). However, states with faster escape rates tend to exhibit slightly lower FRET efficiency. These Iso-I states transition with a single Iso-II state ($E \sim 0.25$) characterized by a ~ 10 s^{-1} escape rate. The transition density heatmap confirms that the major transitions occur between these two main states.

The second trace (Fig. 3c(ii)) shows four interconversions between class I and class V within the 50 s observation window. In the corresponding escape rate trajectory and heatmap, higher escape rates are observed during the transitions between Iso-I and Iso-II. The Iso-I state ($E \sim 0.6$) exhibits a strong escape rate density at $\lambda_{\text{Iso-I}} \sim 0.5$ s^{-1}, while the Iso-II state ($E \sim 0.3$) shows a prominent density at $\lambda_{\text{Iso-II}} \sim 2$ s^{-1}. The transition density heatmap confirms that the dominant transitions occur between these two conformations.

In the third trace (Fig. 3c(iii)), five interconversions between class I ($E \sim 0.6$, $\lambda_{\text{Iso-I}} \sim 0.5$ s^{-1}) and class V ($E \sim 0.3$, $\lambda_{\text{Iso-II}} \sim 0.5$ s^{-1}) are clearly visible and separated by green dashed lines. The presence of intermediate transition states ($0.3 < E < 0.6$) is supported by multiple hotspots in the transition density heatmap, and these states exhibit faster escape rates in the range 5 s$^{-1} < \lambda_{\text{transition}} < 10$ s^{-1}.

The fourth trace (Fig. 3c(iv)) shows ten interconversions between class I and faster-switching conformation classes (II and III). The Iso-I state in these fast-switching classes has a slightly lower FRET efficiency ($E \sim 0.6$) than the class I Iso-I conformation ($E \sim 0.7$), as observed in the escape rate heatmap. Transitions between the two Iso-I states are visible as faint hotspots in the transition density heatmap, alongside the dominant Iso-I and Iso-II transitions.

A more complex dynamic behavior is seen in the fifth trace (Fig. 3c(v)), where the molecule interconverts between class I, class V, and class II. Multiple clusters in the escape rate plot for both Iso-I and Iso-II suggest dynamic heterogeneity under four-way tension forces. Additionally, Iso-II states with slower escape rates tend to exhibit lower FRET efficiencies, which suggests the presence of distinct energy levels. This observation is consistent with the behavior previously noted for Iso-I in the first and fourth traces.

In the sixth trace (Fig. 3c(vi)), a distinct transition state appears at $E \sim 0.5$, visible in the smFRET trajectory, escape rate heatmap, and transition density heatmap. This state exists alongside clear interconversions between class I and class V.

Together, these examples demonstrate that four-way tension forces enable J7 HJs to explore a broader conformational energy landscape, facilitating multiple interconversions between dynamic classes within the 50 s observation window. This is likely due to simultaneous pulling on all four arms by entropic springs, allowing access to a wide range of force directions and conformational pathways. Such interconversions are not observed under tension-free, single-axial tension, or even three-way tension conditions.

In contrast, Hyeon et al.[40] reported that only a single interconversion event could be induced by removing Mg^{2+} from the buffer and then reintroducing it. In our study, we achieve multiple stochastic interconversions under equilibrium buffer conditions containing 12.5 mM Mg^{2+}, simply by applying multi-axial tension in two dimensions.

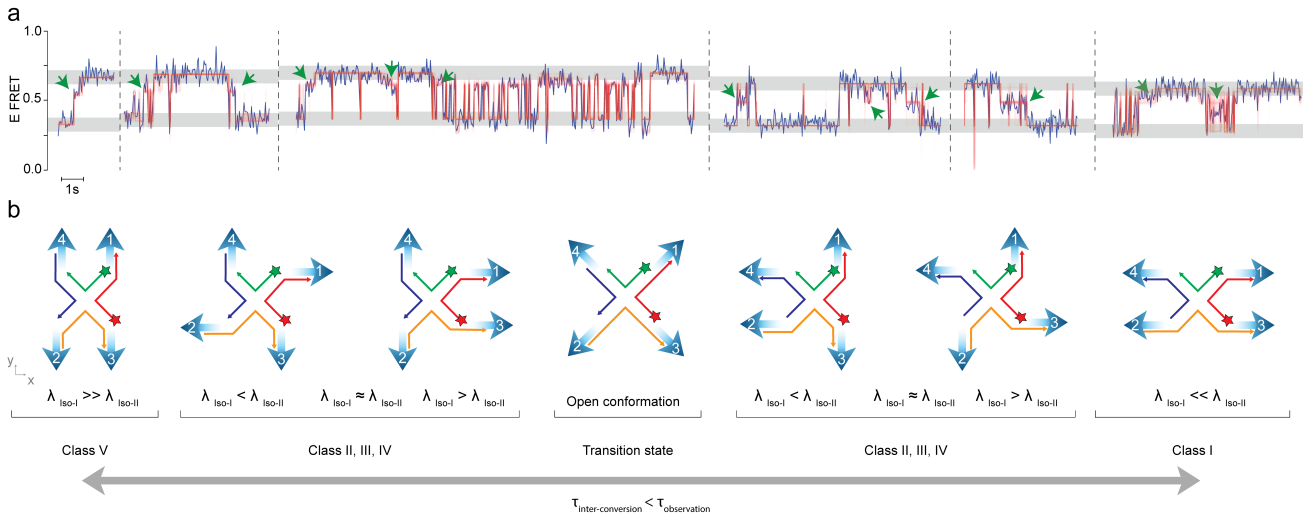

Fig. 4 Transition states under four-way tension forces and proposed entropic spring modes underlying observed smFRET classes and interconversions. (**a**) Zoomed-in regions of several smFRET trajectories (blue curves) shown in Fig. 3c and corresponding BNP-FRET trajectories (red curves), superimposed near interconversion events. Green arrows indicate observed transition states likely stabilized due to enhanced lifetimes under multi-axial tension of four-way tension forces. Grey-shaded bands with a height of $E = 0.1$ highlight the FRET efficiency ranges corresponding to the canonical Iso-I and Iso-II conformations; observed transition states fall outside these ranges. (**b**) Example modes of entropic spring configurations in the four-way tension setup that give rise to the five smFRET trace classes and facilitate multiple interconversions within the 50 s observation time.

Four-way tension stabilizes the HJ transition state and drives class interconversion through diverse pulling modes. The open or unstacked conformation of the HJ corresponds to the transition state during switching between the two stacked antiparallel conformations, Iso-I and Iso-II. Under buffer conditions containing only monovalent cations, this open state is readily detected using gel electrophoresis and smFRET.[34,52] However, in the presence of high divalent cations such as magnesium or calcium, the open conformation becomes extremely short-lived and typically persists for less than one time bin (80 ms) in our experiments, making it very challenging to observe.[53] As such, under tension-free or single-axial tension conditions, such rarely occurring intermediate signals that fall between the typical FRET efficiencies of Iso-I and Iso-II are frequently mischaracterized as noise due to high uncertainty.

The four-way tension configuration, however, can facilitate stabilization of the open state in a buffer containing high divalent cations by applying forces on all four arms of the HJ in a way that prolongs its lifetime. To investigate this, we analyzed the smFRET trajectories and focused on the regions surrounding interconversion events (Fig. 4a).

Using the BNP-FRET framework, which accounts for camera noise and background signal fluctuations during the inference of HMM trajectories, we confidently identified intermediate smFRET states between Iso-I and Iso-II. These states, indicated by green arrows, represent direct observations of the open conformation under divalent ion conditions (Fig. 4a). In some cases, the lifetime of this transition state extends up to ~ 1 s.

Our confidence in identifying these transition states stems from the combined use of MAESTRO's four-way tension and the robustness of the BNP-FRET approach. Since our analysis explicitly incorporates potential noise and background fluctuations,[47,54,55] we can confidently rule out these factors as explanations for the intermediate smFRET values observed. Unlike random noise, which typically persists for only 1–2 experimental time bins (each 40 ms), the observed middle states persist significantly longer and occur repeatedly across multiple trajectories. This strongly indicates that they represent real open conformations.

Based on these observations, we propose that interconversion between smFRET classes is driven by distinct pulling modes of the four entropic springs. Several representative examples of these modes are

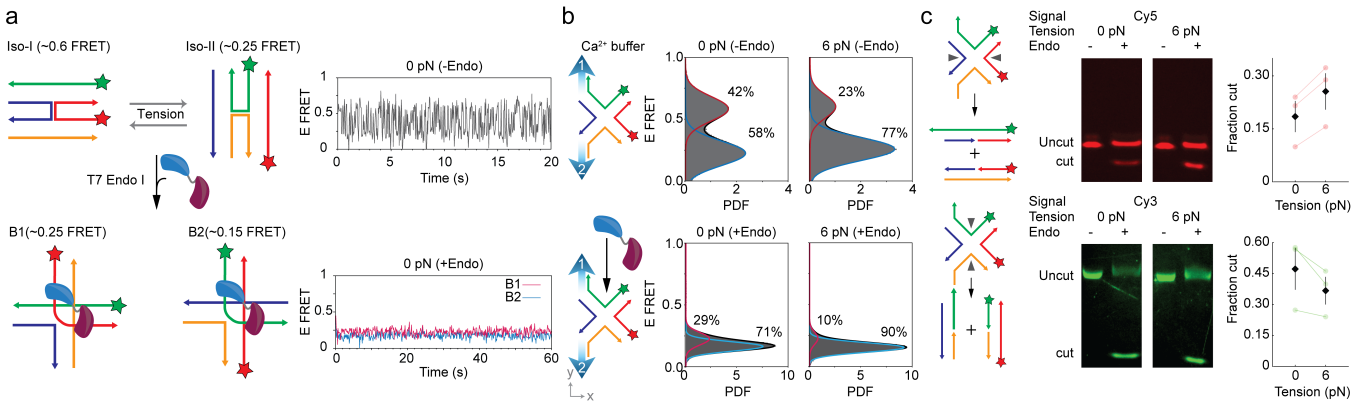

Fig. 5 HJ binding conformations with T7 Endonuclease I and resolution under single-axial tension. (**a**) Schematic of HJ isomers that may be preferentially stabilized by applied tension, along with the binding conformations of HJ with T7 Endonuclease I. Representative smFRET traces are shown in Ca^{2+} buffer for isomer-I, isomer-II, and two bound states (B1 and B2). (**b**) smFRET ensemble histograms of HJ under 0 pN and 6 pN tension along the y-axis, without (top) and with (bottom) T7 Endonuclease I in Ca^{2+} buffer ($n > 140$). (**c**) Left: Two possible HJ resolution pathways involving cleavage of the Cy3- or Cy5-labeled strands. Middle: Representative denaturing PAGE gels imaged under fluorescence channels specific to Cy5 (top) and Cy3 (bottom), showing results under 0 pN and 6 pN tension, with and without T7 Endonuclease I. Right: Quantification of cleavage fractions for Cy3- and Cy5-labeled strands from $n = 3$ independent gel runs (red and green plots), with corresponding mean and standard deviation shown in black, based on ratiometric intensity analysis.

illustrated in Fig. 4b. class V likely emerges when the springs harmonically exert tension forces along the y-axis, whereas class I arises from coordinated pulling along the x-axis. The open conformation appears to be stabilized when all four springs pull in directions that align with the axes of the open state. Other configurations, in which the forces are more balanced between the x and y-axes, give rise to classes II, III, and IV. These pulling modes may fluctuate stochastically due to thermal motion, allowing the HJ to transition between different dynamic states and facilitating multiple class interconversions within the 50 s observation window.

Tension alters J7 HJ binding conformation with T7 Endonuclease I and modulates resolution fidelity. Building on our previous results showing that single-axial tension can shift the equilibrium between HJ isomers (Fig. 2), we investigated whether such tension also affects the binding conformation of T7 Endonuclease I. T7 Endonuclease I is known to interact with HJs in two distinct conformations, termed B1 and B2.[32,34,36] In our experiments, B1 exhibited a FRET efficiency of $E \sim 0.15$, and B2 showed $E \sim 0.25$ (Fig. 5a). Representative smFRET traces under 0 pN tension in Ca^{2+} buffer, both in the presence and absence of T7 Endonuclease I, are shown for comparison.

We observed that the distribution of HJ isomers remains sensitive to single-axial tension applied along the y-axis, even in Ca^{2+} buffer. Increasing the tension from 0 to 6 pN shifts the smFRET histogram towards Iso-II (Fig. 5b, top panel). Upon addition of T7 Endonuclease I, the histogram transitions to show a mixture of B1 and B2 conformations (Fig. 5b, bottom panel), with noticeable changes in their relative populations under 6 pN tension. These findings suggest that tension-induced changes in HJ isomer populations are translated into altered binding conformations of the enzyme. To assess whether tension also affects HJ resolution by T7 Endonuclease I, we employed a denaturing PAGE gel-shift assay to monitor cleavage of DNA strands labeled with Cy3 and Cy5. Resolution can proceed via two scenarios: in one, the enzyme cleaves the green and orange strands; in the other, it cleaves the red and blue strands (Fig. 5c, left panel).

In the absence of T7 Endonuclease I, Cy3- and Cy5-labeled strands remained intact across both tension conditions, appearing as single uncut bands (Fig. 5c, middle panel, Endo (–) lanes). Upon enzyme addition, distinct lower bands corresponding to cleaved products emerged in both fluorescence channels (Endo (+)

lanes), confirming successful HJ resolution. We quantified the band intensities and performed ratiometric analysis to calculate the fraction of cleaved strands (Fig. 5c, right panel). Under 6 pN tension, the fraction of cut Cy5-labeled strands increased compared to the 0 pN condition, while the fraction of cut Cy3-labeled strands decreased. These results suggest that mechanical tension not only influences binding conformations of T7 Endonuclease I but also plays a role in directing the outcome of HJ resolution.

Discussion

We have introduced MAESTRO as a molecular tool to study single-molecule biophysics under multi-axial tension. Our work with MAESTRO exploits rigid 3D DNA origami with circular symmetry and ssDNA entropic spring to exert multi-axial tension on biomolecules of interest, adding more capability to the previous DNA origami force spectroscopy device which can only apply single-axial tension.[11,56] We demonstrated the versatility of MAESTRO to apply different numbers of pulling points from 2, 3, to 4 in the case of single-axial tension, 3-way, or 4-way tension forces, respectively. More pulling directions can be employed if the molecules of interest need more pulling attachments. We have demonstrated such a capability by binding at least 8 points to the inner sidewalls of MAESTRO and confirmed using super-resolution DNA-PAINT imaging. Multi-axial tension capability achieved through MAESTRO are challenging to achieve with conventional force spectroscopy techniques such as optical and magnetic tweezers, which are limited to single-axis force application.[21–23] Finally, with MAESTRO, we have shown high-throughput smFRET study of the dynamics of hundreds of HJ molecules under multi-axial tension.

HJ is well known to show molecule-to-molecule variations in terms of dynamics at 0 pN which we clearly observed in our experiments,[40] demonstrating that MAESTRO has negligible effect on such variations. Furthermore, our study of HJ dynamics under several tension configurations not only agrees with previously published results on pulling HJ in single direction with optical tweezers[18] and DNA origami force spectroscopy device ,[11] but also reveals previously unseen diverse dynamics when moving from single-directional to 3-way or 4-way tension. Furthermore, we observed dynamic and stochastic inter-conversion between several HJ smFRET trace classes under 4-way tension, which could not be achieved previously using state-of-the-art methods,[11,18] showing the significance of studying biomolecules under multi-axial tension. Importantly, such inter-conversions suggest that multi-axial tension forces facilitate the rearrangement of loop-forming sequences near the junction. Such a multiplicity of loop configurations correspond to different energy levels in the energy landscape of conformations, appearing as kinetic heterogeneity in smFRET trajectories.[40]

Our smFRET results on T7 Endonuclease I binding to Holliday junctions under tension suggest a correlation between specific HJ isomers and preferred binding conformations. This relationship is further supported by the gel assay data, which showed opposing trends in the fraction cut between the DNA strands labeled with Cy3 and Cy5. Together, these findings suggest that mechanical tension may introduce a bias in binding conformation and HJ resolution, potentially impacting genetic diversity. This mechanism is consistent with various biologically relevant systems in which tension favors specific conformations that influence downstream processes. For example, in mechanosensitive protein complexes such as focal adhesions (FA), proteins such as integrin, vinculin, and talin undergo tension-induced conformational changes that stabilize the FA complex.[57,58] Similarly, DNA and RNA processing enzymes can experience tension-dependent activity changes; for example, transcription or translocation can stall when nucleic acids are subjected to forces above a critical threshold.[16,59]

Although we demonstrated interconversion driven by multi-axial tension in a relatively simple HJ system, the implications extend to more complex mechanosensitive systems with richer conformational landscapes. In such systems, multi-axial tension may accelerate transitions between inactive and active states, especially for proteins that rely on tension-sensitive conformational changes. Given MAESTRO's size, many such proteins with size < 25 nm can be studied. For example, ion channel membrane proteins are known to experience membrane tension from multiple directions, which can trigger switching between closed (inactive) and open (active) conformations.[60] These multidirectional forces cannot be accurately modeled using single-directional tension alone. Another relevant case is integrin, a dimeric transmembrane protein that

functions as a force receptor and transducer.[27] Its two intracellular tails are anchored to the membrane, with one tail subject to pulling forces from the actomyosin complex, while the ectodomain binds to the extracellular matrix.[27] These distinct connections expose integrin to multi-directional forces that are essential for regulating its conformational activation and downstream signaling pathways. Intrinsically disordered protein (IDP) is another class of proteins that can benefit from MAESTRO. Larger proteins can also be accommodated by constructing MAESTRO with a larger diameters using multi-scaffolding DNA origami.[61] Finally, using single-photon detectors, MAESTRO can be used to potentially study the really fast micro to millisecond scale dynamics of mechanosensitive molecules under tension.[62] Given the versatility of MAESTRO, and its ability to apply and fine-tune multiaxial forces, we anticipate that it will be a valuable tool to probe the dynamics of such mechanosensitive systems.

Funding

The research was funded by the National Science Foundation (NSF) through NSF career (MCB 2341002) for R.F. Hariadi. S. Presse acknowledges support from the National Institutes of Health (NIH) (R01GM134426, R01GM130745, R35GM148237), and US Army (ARO (W911NF-23-1-0304)). G. B. M. Wisna is supported by an American Heart Association (AHA) predoctoral fellowship (23PRE1029870).

Acknowledgements

The authors thank Chenxiang Lin for the Cadnano file of the cylindrical DNA origami and for discussions. We acknowledge the use of facilities within the Eyring Materials Center as well as Phoenix and Sol supercomputers at Arizona State University.

Correspondence

All correspondence and requests for materials should be addressed to R.F. Hariadi.

References

1. Phillips R, Kondev J, Theriot J, Garcia H (2012) *Physical biology of the cell.* (Garland Science).
2. Bustamante CJ, Chemla YR, Liu S, Wang MD (2021) Optical tweezers in single-molecule biophysics. *Nature Reviews Methods Primers* 1:25.
3. Tapia-Rojo R, Mora M, Garcia-Manyes S (2024) Single-molecule magnetic tweezers to probe the equilibrium dynamics of individual proteins at physiologically relevant forces and timescales. *Nature Protocols* 19:1779.
4. Rief M, Oesterhelt F, Heymann B, Gaub HE (1997) Single molecule force spectroscopy on polysaccharides by atomic force microscopy. *Science* 275:1295.
5. Yang D, Ward A, Halvorsen K, Wong WP (2016) Multiplexed single-molecule force spectroscopy using a centrifuge. *Nature Communications* 7:11026.
6. Zhang Y, Ge C, Zhu C, Salaita K (2014) DNA-based digital tension probes reveal integrin forces during early cell adhesion. *Nature Communications* 5:5167.
7. Wang X, Ha T (2013) Defining single molecular forces required to activate integrin and notch signaling. *Science* 340:991.
8. Jo MH, et al. (2024) Determination of single-molecule loading rate during mechanotransduction in cell adhesion. *Science* 383:1374.
9. Jo MH, et al. (2022) Single-molecule characterization of subtype-specific $\beta 1$ integrin mechanics. *Nature Communications* 13:7471.
10. Choi B, Zocchi G, Wu Y, Chan S, Jeanne Perry L (2005) Allosteric control through mechanical tension. *Phys. Rev. Lett.* 95(7):078102.
11. Nickels PC, et al. (2016) Molecular force spectroscopy with a DNA origami–based nanoscopic force clamp. *Science* 354:305.
12. Hellenkamp B, et al. (2018) Precision and accuracy of single-molecule FRET measurements—a multi-laboratory benchmark study. *Nature Methods* 15:669.
13. Yasuda R, Noji H, Kinosita K, Yoshida M (1998) F1-ATPase is a highly efficient molecular motor that rotates with discrete 120 steps. *Cell* 93:1117.

14. Altman D, Sweeney HL, Spudich JA (2004) The mechanism of myosin VI translocation and its load-induced anchoring. *Cell* 116:737.
15. Svoboda K, Block SM (1994) Force and velocity measured for single kinesin molecules. *Cell* 77:773.
16. Wuite GJ, Smith SB, Young M, Keller D, Bustamante C (2000) Single-molecule studies of the effect of template tension on T7 DNA polymerase activity. *Nature* 404:103.
17. Abraham Punnoose J, et al. (2023) High-throughput single-molecule quantification of individual base stacking energies in nucleic acids. *Nature Communications* 14:631.
18. Hohng S, et al. (2007) Fluorescence-force spectroscopy maps two-dimensional reaction landscape of the Holliday junction. *Science* 318:279.
19. Yu H, Siewny MG, Edwards DT, Sanders AW, Perkins TT (2017) Hidden dynamics in the unfolding of individual bacteriorhodopsin proteins. *Science* 355:945.
20. Bustamante C, Alexander L, Maciuba K, Kaiser CM (2020) Single-molecule studies of protein folding with optical tweezers. *Annual Review of Biochemistry* 89:443.
21. Neuman KC, Nagy A (2008) Single-molecule force spectroscopy: optical tweezers, magnetic tweezers and atomic force microscopy. *Nature Methods* 5:491.
22. Dulin D, et al. (2015) High spatiotemporal-resolution magnetic tweezers: calibration and applications for DNA dynamics. *Biophysical Journal* 109:2113.
23. Moffitt JR, Chemla YR, Smith SB, Bustamante C (2008) Recent advances in optical tweezers. *Annual Reviews of Biochemistry* 77:205.
24. Geiger B, Spatz JP, Bershadsky AD (2009) Environmental sensing through focal adhesions. *Nature Reviews Molecular Cell Biology* 10:21.
25. Kanchanawong P, et al. (2010) Nanoscale architecture of integrin-based cell adhesions. *Nature* 468:580.
26. Giancotti FG, Ruoslahti E (1999) Integrin signaling. *Science* 285:1028.
27. Campbell ID, Humphries MJ (2011) Integrin structure, activation, and interactions. *Cold Spring Harbor Perspectives in Biology* 3:a004994.
28. Rothemund PW (2006) Folding DNA to create nanoscale shapes and patterns. *Nature* 440:297.
29. Dietz H, Douglas SM, Shih WM (2009) Folding DNA into twisted and curved nanoscale shapes. *Science* 325:725.
30. Smith SB, Cui Y, Bustamante C (1996) Overstretching B-DNA: the elastic response of individual double-stranded and single-stranded DNA molecules. *Science* 271:795.
31. Fisher PDE, et al. (2018) A programmable DNA origami platform for organizing intrinsically disordered nucleoporins within nanopore confinement. *ACS Nano* 12:1508.
32. Hadden JM, Déclais AC, Carr SB, Lilley DM, Phillips SE (2007) The structural basis of Holliday junction resolution by T7 endonuclease I. *Nature* 449:621.
33. Ortiz-Lombardía M, et al. (1999) Crystal structure of a DNA Holliday junction. *Nature Structural Biology* 6:913.
34. Zhou R, et al. (2019) Junction resolving enzymes use multivalency to keep the Holliday junction dynamic. *Nature Chemical Biology* 15:269.
35. Biertümpfel C, Yang W, Suck D (2007) Crystal structure of T4 endonuclease VII resolving a Holliday junction. *Nature* 449:616.
36. Déclais AC, et al. (2003) The complex between a four-way DNA junction and T7 endonuclease I. *The EMBO Journal*.
37. Wyatt HD, West SC (2014) Holliday junction resolvases. *Cold Spring Harbor Perspectives in Biology* 6:a023192.
38. McKinney SA, Déclais AC, Lilley DM, Ha T (2003) Structural dynamics of individual Holliday junctions. *Nature Structural Biology* 10:93.
39. Karymov M, Daniel D, Sankey OF, Lyubchenko YL (2005) Holliday junction dynamics and branch migration: single-molecule analysis. *Proceedings of the National Academy of Sciences* 102:8186.
40. Hyeon C, Lee J, Yoon J, Hohng S, Thirumalai D (2012) Hidden complexity in the isomerization dynamics of Holliday junctions. *Nature Chemistry* 4:907.
41. Grainger RJ, Murchie AI, Lilley DM (1998) Exchange between stacking conformers in a four-way DNA junction. *Biochemistry* 37:23.
42. Li X, Heyer WD (2008) Homologous recombination in DNA repair and DNA damage tolerance. *Cell Research* 18:99.
43. Cromie GA, et al. (2006) Single Holliday junctions are intermediates of meiotic recombination. *Cell* 127:1167.
44. Mitchel K, Zhang H, Welz-Voegele C, Jinks-Robertson S (2010) Molecular structures of crossover and noncrossover intermediates during gap repair in yeast: implications for recombination. *Molecular Cell* 38:211.
45. Clapier CR, Cairns BR (2009) The biology of chromatin remodeling complexes. *Annual Review of Biochemistry* 78:273.

46. Nettels D, et al. (2024) Single-molecule FRET for probing nanoscale biomolecular dynamics. *Nature Reviews Physics* 6:587.
47. Saurabh A, Wisna GBM, Schwieger M, Hariadi R, Presse S (2025) Bayesian nonparametrics for FRET using realistic integrative detectors. *Biorvix*.
48. Schnitzbauer J, Strauss MT, Schlichthaerle T, Schueder F, Jungmann R (2017) Super-resolution microscopy with DNA-PAINT. *Nature Protocols* 12:1198.
49. Hart DJ, Jeong J, Gumbart JC, Kim HD (2023) Weak tension accelerates hybridization and dehybridization of short oligonucleotides. *Nucleic Acids Research* 51:3030.
50. Jungmann R, et al. (2010) Single-molecule kinetics and super-resolution microscopy by fluorescence imaging of transient binding on DNA origami. *Nano Letters* 10:4756.
51. Lilley DM (2000) Structures of helical junctions in nucleic acids. *Quarterly Reviews of Biophysics* 33:109.
52. Duckett DR, et al. (1988) The structure of the Holliday junction, and its resolution. *Cell* 55:79.
53. Joo C, McKinney SA, Lilley DM, Ha T (2004) Exploring rare conformational species and ionic effects in DNA Holliday junctions using single-molecule spectroscopy. *Journal of molecular biology* 341(3):739.
54. Saurabh A, Safar M, Fazel M, Sgouralis I, Pressé S (2023) Single-photon smFRET: II. Application to continuous illumination. *Biophysical Reports* 3.
55. Saurabh A, Fazel M, Safar M, Sgouralis I, Pressé S (2023) Single-photon smFRET. I: Theory and conceptual basis. *Biophysical Reports* 3.
56. Kramm K, et al. (2020) DNA origami-based single-molecule force spectroscopy elucidates RNA Polymerase III pre-initiation complex stability. *Nature Communications* 11:2828.
57. Grashoff C, et al. (2010) Measuring mechanical tension across vinculin reveals regulation of focal adhesion dynamics. *Nature* 466:263.
58. Tapia-Rojo R, Alonso-Caballero A, Fernandez JM (2020) Direct observation of a coil-to-helix contraction triggered by vinculin binding to talin. *Science Advances* 6:eaaz4707.
59. Yin H, et al. (1995) Transcription against an applied force. *Science* 270:1653.
60. Lee AG (2004) How lipids affect the activities of integral membrane proteins. *Biochimica et Biophysica Acta (BBA)-Biomembranes* 1666:62.
61. Engelhardt FA, et al. (2019) Custom-size, functional, and durable DNA origami with design-specific scaffolds. *ACS nano* 13(5):5015.
62. Lerner E, et al. (2021) FRET-based dynamic structural biology: Challenges, perspectives and an appeal for open-science practices. *Elife* 10:e60416.
63. Zadeh JN, et al. (2011) NUPACK: Analysis and design of nucleic acid systems. *Journal of Computational Chemistry* 32:170.
64. Kapanidis AN, et al. (2004) Fluorescence-aided molecule sorting: analysis of structure and interactions by alternating-laser excitation of single molecules. *Proceedings of the National Academy of Sciences* 101:8936.

Materials and methods

Materials. Unmodified and biotinylated DNA staple strands for DNA origami MAESTRO were purchased from Integrated DNA Technologies (IDT). Scaffold strands (P8064) were sourced from Bayou Biolabs. Amine-modified DNA strands used as imager strands were also obtained from IDT. Cy3B-NHS ester fluorophores (PA63101) were purchased from GE Healthcare. All general chemicals were supplied by Sigma-Aldrich. Glass coverslips (48466-205) and microscope slides (16004-430) were obtained from VWR. Kapton tape (PPTDE-2), used in constructing flow chambers, was acquired from Bertech.

DNA-PAINT Imager strands. Imager strands (TATGTAGATC/3' Cy3B/) were prepared by conjugating amine-modified DNA oligonucleotides with Cy3B fluorophores via NHS ester coupling. The conjugated products were subsequently purified using high-performance liquid chromatography (HPLC).

Tension Force Estimation Using the Modified Freely-Jointed Chain (FJC) Model. We estimated the tension force generated along the ssDNA springs using a modified freely-jointed chain (FJC) polymer model, as described in Eq.1[30]:

$$d = L_{ss}\left[\coth\left(\frac{FL_K}{k_BT}\right) - \frac{k_BT}{FL_K}\right]\left(1+\frac{F}{S}\right), \qquad [1]$$

where d is the end-to-end distance of the ssDNA spring (45 nm for MAESTRO), $L_{ss} = Nl_{nt}$ is the total contour length of the ssDNA entropic spring with N is the number of nucleotides, l_{nt} is the contour length per nucleotide (0.6–0.7 nm), F is the applied tension, k_B is the Boltzmann constant, T is the temperature, and L_K is the Kuhn length (1.5 nm).[30]

To realize the desired tension values, we extend selected staple strands on MAESTRO with uniquely designed ssDNA spring sequences at defined positions. These sequences are designed using NUPACK[63] to minimize both self-interaction and cross-interaction between springs—critical design considerations for maintaining predictable force application in multi-axial configurations (Fig. S5 and Table S1). Preventing such interactions ensures consistency with the assumptions of the FJC model, which treats the polymer chain as composed of non-interacting monomers.

MAESTRO Folding and Purification. To assemble DNA origami MAESTRO structures, P8064 scaffold strands were mixed with staple strands, biotinylated strands, and corresponding entropic spring strands in 1× TAE buffer containing 12.5 mM Mg^{2+} (see Table S1 and S3). The scaffold was used at a concentration of 20 nM, while staple and entropic spring strands were added at a 10-fold molar excess relative to the scaffold. The mixture was annealed by heating to 80° C for 5 minutes, followed by a gradual cooling to 4° C at a rate of 3 minutes and 12 seconds per degree Celsius. Following annealing, the folded DNA origami structures were purified through five rounds of centrifugal filtration using Amicon Ultra-0.5 devices with a 100 kDa molecular weight cut-off.

Negative-Stain Transmission Electron Microscopy of MAESTRO. Amicon-purified MAESTRO samples were diluted to a final concentration of 2 nM in 1× TAE buffer supplemented with 12.5 mM $MgCl_2$. Carbon-coated TEM grids (Tedpella 01814-F) were glow-discharged for 30–60 s prior to sample application. A 10 µL aliquot of the diluted sample was applied to the grid and incubated for 1–2 minutes. Excess liquid was gently wicked off using Whatman filter paper.

Without allowing the grid to dry, 10 µL of a 2% (w/v) aqueous uranyl acetate solution containing 25 mM NaOH was applied and immediately wicked away. A second 10 µL aliquot of the same staining solution was added and incubated on the grid for 30–60 s before removal. Grids were then air-dried completely prior to imaging.

Negative-stained samples were imaged using a Talos L120C G2 transmission electron microscope operated at 120 kV with a magnification of 57,000×.

Holliday Junction (HJ) Formation HJ samples were prepared by mixing four single-stranded DNA (ssDNA) oligonucleotides at equal molar concentrations. Specific strand extensions were included on selected strands depending on the desired tension configuration (two-way, three-way, or four-way; see Table S2). The strands were diluted in buffer to a final concentration of 1× TAE supplemented with 12.5 mM $MgCl_2$. The mixture was annealed by heating to 80° C for 5 minutes, followed by gradual cooling to 4° C at a rate of 3 minutes and 12 seconds per degree Celsius.

DNA-PAINT Super-Resolution Imaging for Short Oligo Tension Studies and Data Processing. MAESTRO structures bearing different ssDNA entropic springs corresponding to defined tension values were first folded and purified. These were then mixed with short docking oligos at equimolar concentrations and incubated at room temperature for at least 3 hours to allow hybridization of the docking strands (Table S1) to the ssDNA springs (spring-1 and spring-2).

DNA-PAINT super-resolution imaging was performed following protocols established by Schnitzbauer et al.[48] In brief, MAESTRO structures either bearing 8 docking sites on their inner sidewalls (Fig. 1e, right panel and Fig. S6) or incorporating short oligos under defined mechanical tension (Fig. 1g, left panel; Table S3 and S4) were immobilized onto coverslips coated with BSA-biotin and streptavidin. Coverslips were assembled into flow chambers using standard glass microscope slides and double-sided Kapton tape.

For surface preparation, BSA-biotin and streptavidin were diluted to final concentrations of 1 mg/mL and 0.5 mg/mL, respectively, in Buffer A+ (10 mM Tris-HCl, 100 mM NaCl, 0.05% (v/v) Tween 20, pH 8.0). MAESTRO samples were diluted to 2 nM in Buffer B+ (5 mM Tris-HCl, 12.5 mM $MgCl_2$, 1 mM EDTA, 0.05% (v/v) Tween 20, pH 8.0), which was also used to prepare the imager strand solution (TATGTAGATC/3' Cy3B/). The final imaging buffer contained an oxygen scavenging system comprising 1.25× PCA, 1× PCD, and 1× Trolox, along with 5 nM imager strands. The flow chamber was sealed with epoxy before imaging.

Imaging was conducted using an Oxford Nanoimager (ONI) Benchtop Nanoimager S Mark II equipped with total internal reflection fluorescence (TIRF) microscopy. Cy3B fluorophores were excited with a 532 nm laser at power densities between 800 and 1250 W/cm^2, and emission was collected using a 549–623 nm bandpass filter. A 100× oil-immersion Olympus objective (NA 1.49) was used, and images were captured with a Hamamatsu ORCA-Flash4.0 V3 sCMOS camera at exposure time per frame of 200 ms for the DNA-PAINT movies of MAESTRO constructs with 8 docking sites and of 100 ms for the short oligos under tension studies. The system featured z-lock autofocus and a piezo-controlled stage for precise positioning. All data were collected at room temperature (23∘ C).

DNA-PAINT movies of MAESTRO constructs with 8 docking sites were analyzed using Picasso software for localization, rendering, and generation of averaged images from 412 MAESTRO molecules[48]. Binding and unbinding durations were extracted from the image stacks using a custom Python script. To estimate λ_{on} and λ_{off}, the distributions of bright and dark times were fitted using the cumulative distribution function (CDF) of an exponential distribution (Fig. S2):

$$\text{CDF}(t) = 1 - \exp(-\lambda t) \qquad [2]$$

To analyze the force dependence of oligo binding kinetics, we fit the experimental data using models from Hart et al.,[49] given by:

$$k_{\text{off}}(F) = k_{\text{off}}(0) \exp\left[\frac{F\Delta x_{\text{off}}}{k_B T}\right], \qquad [3]$$

$$k_{\text{on}}(F) = k_{\text{on}}(0) \exp\left[\frac{\int_0^F \left(\frac{f}{a} + b\right) df}{k_B T}\right], \qquad [4]$$

Here, k_B is the Boltzmann constant, and T is the temperature. Parameters $k_{\text{off}}(0)$ and $k_{\text{on}}(0)$ represent the dissociation and association rates at $F = 0$ pN, respectively. Δx_{off} denotes the extension difference between the transition and bound states. Parameters a and b represent the differences in stiffness and relaxed extension between the unbound and transition states. Fitted parameter values are summarized in Table S5.

smFRET of HJs Under Tension. MAESTRO constructs incorporating various single-stranded DNA (ssDNA) entropic springs, designed to generate specific tension magnitudes and configurations, were folded and purified. Corresponding HJ samples for each tension configuration were prepared separately. MAESTRO and HJ samples were then mixed in equal volumes to achieve a final concentration of 5 nM each and incubated at room temperature on a shaker (400 rpm) for at least 4 hours to allow hybridization between the HJ extensions and the ssDNA springs.

smFRET samples were prepared on a coverslip assembled into a flow chamber using a glass microscope slide and double-sided Kapton tape. Surface functionalization was performed by sequentially introducing BSA-biotin and streptavidin, diluted to final concentrations of 1 mg/mL and 0.5 mg/mL, respectively, in Buffer A+ (10 mM Tris-HCl, 100 mM NaCl, 0.05% (v/v) Tween 20, pH 8.0). The MAESTRO–HJ complex was diluted to 2 nM in Buffer B+ (5 mM Tris-HCl, 12.5 mM $MgCl_2$, 1 mM EDTA, 0.05% (v/v) Tween 20, pH 8.0) and immobilized onto the functionalized coverslip.

Sample introduction into the flow chamber followed this sequence: 20 μL of BSA-biotin, a Buffer A+ wash, streptavidin, a second Buffer A+ wash followed by Buffer B+, the MAESTRO–HJ complex, a final Buffer B+ wash, and then the imaging buffer. Each step was incubated for 2 minutes. The imaging buffer consisted of Buffer B+ supplemented with an oxygen scavenging system containing 1.25× PCA, 1× PCD, and 1× Trolox. The flow chamber was sealed with epoxy prior to imaging.

smFRET imaging was performed on an Oxford Nanoimager (ONI) Benchtop Nanoimager S Mark II equipped with total internal reflection fluorescence (TIRF) optics. Alternating laser excitation (ALEX) was used to sequentially excite the green (532 nm) and red (638 nm) lasers, synchronized with camera acquisition. Each excitation had a 20 ms exposure, resulting in an effective binning time of 40 ms. A total of 5,000 frames were acquired per field of view. Imaging was conducted using a 100× oil-immersion Olympus objective (NA 1.49), and fluorescence was captured with a Hamamatsu ORCA-Flash4.0 V3 sCMOS camera. Green laser power densities ranged from 115–340 W/cm^2, while red laser power ranged from 75–240 W/cm^2. The microscope was equipped with a z-lock autofocus system and a piezo-controlled stage for high-precision imaging. All data were collected at room temperature (23∘ C).

smFRET of HJs Under Tension with T7 endonuclease I The preparation of MAESTRO–HJ samples followed the same protocol described in the smFRET of HJs Under Tension section, with one key modification: all buffers were prepared using 1× TAE containing 50 mM NaCl and 12.5 mM $CaCl_2$ instead of $MgCl_2$ to prevent cleavage of HJs by T7 endonuclease I.[34]

A final concentration of 2 nM MAESTRO–HJ complex was mixed with T7 endonuclease I (New England Biolabs, catalog no. M0302L) at a final amount of 50 Units (22.5 ng) in a 20 μL total reaction volume, yielding an enzyme concentration of approximately 18.7 nM. The mixture was incubated at room temperature for at least 10 minutes to allow the enzyme to bind to the HJs prior to sample introduction into the flow chamber.

Flow chamber preparation and flow steps followed the same procedure as described in the smFRET of HJs Under Tension section, with buffer B+ replaced with C+ containing 10 mM Tris-HCl, 50 mM NaCl, 12.5 mM $CaCl_2$, 0.05% (v/v) Tween 20 and -containing buffers to prevent the cleavage.

The smFRET imaging protocol was also identical to the standard method, with a slight modification in camera exposure time. For control experiments without T7 endonuclease I (Fig. 5b, top panel), a 20 ms exposure per frame was used. For samples containing T7 endonuclease I, the exposure time was increased to 60 ms (Fig. 5b, bottom panel) to improve the signal-to-noise ratio and enhance resolution between the B1 and B2 smFRET states. All data were collected at room temperature (23∘ C).

HJ Resolution by T7 endonuclease I Assessed via Denaturing PAGE Gel. To investigate the cleavage activity of T7 endonuclease I on HJs under defined tension conditions, we performed an electrophoretic mobility shift assay using a denaturing PAGE gel. A 12% polyacrylamide gel was prepared in the presence of 8 M urea.

MAESTRO DNA origami constructs were prepared to apply two different levels of tension on HJs: 0 pN and 6 pN. As a control, HJs without MAESTRO were also included. All samples were tested in both the presence and absence of T7 endonuclease I.

For the digestion assay, approximately 100 nM of each DNA sample was pre-incubated with 50 Units of T7 endonuclease I in 10 mM Tris-HCl containing 50 mM NaCl and 12.5 mM $CaCl_2$ buffer at room temperature for 15 minutes to allow efficient enzyme binding. The cleavage reaction was initiated by adding the endonuclease reaction buffer, followed by incubation at 30° C for 40 minutes. The reaction was then quenched by the addition of 0.5 M EDTA.

To denature the cleaved DNA fragments, equal volumes of formamide were added to each sample, followed by heating at 90° C for 10 minutes. The denatured samples were loaded onto the gel and electrophoresed for 1 hour at 150 V. After electrophoresis, the gel was imaged using a gel documentation system (Azure Biosystems 300), and the band intensities were analyzed using a custom Mathematica script to quantify the ratio of cleaved to total DNA fragments.

BNP-FRET Analysis The detailed methodology for Bayesian nonparametric FRET (BNP-FRET) analysis is described in Saurabh et al.[47] For each dataset, at least three fields of view were analyzed, with each field consisting of a minimum of 2,500 frames. From these, smFRET traces were extracted from $n > 100$ individual molecules.

To ensure the quality of single-molecule data, several filtering criteria were applied: ALEX stoichiometry filtering,[64] assessment of fluctuations in total donor and acceptor fluorescence during donor excitation, and a minimum requirement of at least one FRET state transition per trace. These filters were used to confirm that only high-confidence single-molecule traces were included in the analysis.

Camera dark noise calibration was performed by acquiring 2,500 frames with the same exposure time as the experimental settings, without laser excitation and in the absence of samples. Local background fluorescence was also subtracted during trace extraction. The filtered and calibrated traces were subsequently analyzed using the BNP-FRET pipeline, executed on the Arizona State University high-performance computing cluster.

Code Availability The BNP-FRET analysis pipeline is available at: https://github.com/LabPresse/BNP-FRET-Binned.

Supporting Information

DNA origami-based platform for multi-axial single-molecule force spectroscopy reveals hidden dynamics in Holliday junctions

Gde Bimananda Mahardika Wisna[a,c,d], **Ayush Saurabh**[a,d], **Ranjan Sasmal**[c], **Deepak Karna**[c], **Prathamesh Chopade**[c], **Steve Pressé**[a,b,d], **and Rizal F. Hariadi**[a,c,d,1]

[a]Department of Physics, Arizona State University, Tempe, Arizona, USA.; [b]School of Molecular Sciences, Arizona State University, Tempe, Arizona, USA.; [c]Center for Molecular Design and Biomimetics at the Biodesign Institute, Arizona State University, Tempe, Arizona, USA.; [d]Center for Biological Physics, Arizona State University, Tempe, Arizona, USA.

[1]To whom correspondence should be addressed. E-mail: rhariadi@asu.edu

Contents

Supplementary Tables **1**
Supplementary Table 1. MAESTRO, DNA-PAINT docking and ssDNA spring strands 1
Supplementary Table 2. HJ strands for various tension forces configuration 6
Supplementary Table 3. MAESTRO mixing concentrations across different tension conditions. . 7
Supplementary Table 4. MAESTRO mixing concentrations for DNA-PAINT assay 8
Supplementary Table 5. Fitted values kinetics parameters for short oligos under tension 8

Supporting Figures **9**
Figure S1: MAESTRO schematics and cadnano design. 9
Figure S2: Histogram plots of bright and dark times of short oligos under various tension forces . 10
Figure S3: Additional examples of smFRET traces from the four-way tension force configuration. 11
Figure S4: Additional examples of smFRET traces from the four-way tension force configuration. 11
Figure S5: Nupack analysis of ssDNA springs. 13
Figure S6: MAESTRO DNA-PAINT schematics and all picked molecules. 14

Name	Sequence	Note
11[196]-4[210]	CAATAGATAAATTAATAGACAAACCCTCAATTGTAGCGA	Core staples
6[447]-14[448]	AGAGGAAGCGCAGACGGTCACAAGAACTGACCTTACGAGAAA	Core staples
14[20]-8[504]	CATCAACTTTTGTTCCATATTTTGTTAAAATTTTGCC	Core staples
4[83]-3[69]	GAGCCGGACTTGTAGAACAGAAACAAAAAATCCCGTAT	Core staples
8[216]-15[223]	AAAGAAGACAGGGAGAAACAATACAGATGATGAGTAACA	Core staples
8[153]-15[160]	TATTACCGCGGTTGTAGCAATACGGTTGCTTAGTGTAGC	Core staples
11[217]-9[226]	GTAAAAACCATAATTCATCAATATATGATTATACG	Core staples
0[90]-8[91]	TGATATTCCCATCCTGTTTGATGGTGCCAGCTGCCTAATCCGGAAGC	Core staples
3[7]-6[7]	TAGCATGTCACCAACGGTAATCGTAGCAAACAATGTATAAG	Core staples
12[272]-11[258]	CACGCTCAACAGTAGGGTTCTGAATTAGATTTTCAGGT	Core staples
14[195]-12[210]	TCCTTGCAGAGAAGTATTAGACTTTACAAACACATCAAAA	Core staples
6[51]-11[48]	CCCGCGGCGAAATGTAAAACGACGGCCAATTAAGTTTCGCTAAGGCTG	Core staples
3[343]-11[342]	AAAGCCCACAAAACCAGAACAGAATCAAGTGTAGCAC	6b position
0[279]-8[280]	TTAAGCAAAAACACCCTGAACAACTAACGAGTTTTGAAGTTTAGCGA	Core staples
6[321]-14[322]	AACAAAGACTATCTTACCGATAAGACGGAATACCGAAACGCA	Core staples
11[70]-4[84]	GCAGGCGCTTTTGCATCAGTGCTGGTCTGGTCAACCAGT	Core staples
14[335]-8[315]	TATAAAACAAAAGAACAGGAAACGCAATAATAAGAAG	Core staples
9[290]-4[294]	TACCGAGGCGTCCTTAAATCAAGATTGAATCTTATTTGCCTCCCAA	Core staples
14[321]-12[336]	AAGACGAAAAGAAAATACATACATAAAGGTGGACAAATCA	Core staples
15[252]-14[273]	AAAGAGGCATTTTCGAGCCAGTAATAAGAGACCAACAA	Core staples
4[272]-3[258]	TTTCTTCTGACCTAAATTTAATTAAGAATTTATCAATA	Core staples
11[133]-4[147]	CCTAAAGGGAAGAAGCACTCCAACGTCAAAGTCAATACG	Core staples
6[177]-11[174]	GGATACCTACATCTATCGGCCTTGCTGGATTAGTAAGTCTGTTGAGAA	Core staples
8[468]-15[475]	CAATACTGAGGACGACGATAAAACGTTGGGATTTAATTT	Core staples
9[416]-4[420]	TAATTAGTTGCGATATATTCGGTCGCGATCGTCGGGTAGCACTTTT	Core staples
11[227]-0[217]	AAATAACAGTAAATAACCGTACATACTATATGGACCCTGTAATACTT	Core staples
11[154]-9[163]	TACGCCAAGGGAGAGCACGTATAACGTACTATTTC	Core staples
4[356]-3[342]	TGATATTAGAATGGTTTGATGATACAGGAGTGTTCTCATT	6a position
11[490]-9[505]	AACGCCAGGTAGAACTAACGGAACATAAGAACGCAAAAGAA	Core staples
11[91]-9[100]	GTCATAAATGCGTGCATCAGACGATCAGCGGTTCG	Core staples
6[195]-14[196]	AATCAAAACACCTCAAATATTTAGAGCTTTAGGAGTATTAAA	Core staples
14[132]-12[147]	GAAAGATGCCTTGACGGGGAAAGCCGGCGAACACTTTTAG	Core staples
15[287]-11[289]	TACCGACAAAAGGTATGTTCAGGATAAGTAATTTACGAGCATTTC	Biotin position
4[293]-3[279]	TCCAAATAATGAAAGACGGGAGAATTAACTGACTTTTAAC	5a position
7[21]-1[16]	CACGGGAACTAAACAGGAAGATGAG	Core staples
4[398]-3[384]	AAAAACATGAAAGTATTGCAGGTCACTGAATTTACCCC	Core staples
0[321]-6[304]	ATTAACAGAGAGATAGAACATAAAAACAGGGAAGTGAGCGCTTTTA	Core staples
3[448]-6[448]	CCATGTTACTTTGAAATCCGCGACCTCGCCTGAACTTTGAA	Core staples
15[315]-14[336]	ACACCACGGAATAAGTTTATTTTGTCACAATTGCAACA	Core staples
3[469]-11[468]	GAGCTTTTCAAAGACTATCTCGTTTACCATACCACAT	8b position
6[258]-14[259]	ATAAGGATATTAATGGTTTGTCTTACTTTAGTATATGTAATT	Core staples
11[164]-0[154]	ATCCCCATCACCCAGTAAATTGGCATAAAACATATTTAAATGCAAT	Core staples
6[384]-14[385]	TTTTGCAAGAAGAGGCTGAGATCACCATATAAGTCCACCACC	Core staples
3[28]-11[27]	TGGGCGCTGCTCGTGGTGAGCTGGCGAAAATAAAGCG	1b position
12[461]-11[447]	AACCCAAATCAACGTAAAAATGAATCTAAAGGAATTGG	Core staples
8[279]-15[286]	ACCTCCCGGTTCATCGTAGGAATAGAACGCGATATAAAG	Core staples
14[272]-8[252]	CGCCAACCATATGCACATTACTAGAAAAAGCCCAAAA	Core staples
11[7]-4[21]	AATAGGAACGGCCAGCTCAGAAAAGCCCCAACCATTTGC	Core staples
12[146]-11[132]	ACGCCCCCGATTTAGAGCTGTGCACCGCGTGCCTGTAC	Core staples
11[301]-9[316]	CAAGAACATCCTCCTGAACAAGAAACGACAATCAAATCAGA	Core staples
9[506]-1[503]	GTTCGAACGAGGCATAGTAATTGCATAAACGAGGCTGAAT	Core staples
9[65]-0[56]	TTCGCCAGCGATCGGTGCGAAAGAGATGTTTACCCGTTTTTGCCGGAG	Core staples
0[216]-8[217]	TTGCGGGACTTTGGGTTATATAAAATCAATACATCAAGACCTGAGCA	Core staples
3[133]-6[133]	TTTGGAACAAGCGTTGAGTGTTGTTAAGAATAGTCTATCAG	Core staples
11[322]-4[336]	TATTACGCAGAGGCATGATAGCCCTTTTTAACCCAAATA	Core staples
8[377]-7[398]	GCCCCCTTTCAGAACCGCCTCAGTACCAGGCGGATAACA	Core staples
15[161]-11[163]	GGTCACGCTGCGCGTAGGGCGCGTGCTTTAGGAGGCCGATTAAGA	Biotin position
14[6]-12[21]	TGAGCTTACCGCGTCTGGCCTTCCTGTAGCCAGGGAAACC	Core staples
0[307]-4[305]	ATCATACAGGCAAGGCGGGTAATCGCATTAATAGCAGCCTTTTAT	Core staples
8[62]-7[83]	CACGACGTCGTACAGCGCGGCAGCACCGTCGGTGGTGAA	Core staples
11[49]-9[64]	CGCAACCTTTCCCAGGAAGATCGCATAGATGGGCCAGGGTT	Core staples
11[28]-9[37]	CCATTCGTGCCGGACGACGACAGTAGCATCTGCAA	Core staples
3[217]-11[216]	TAAGACAAAACATGAGTGCCTTTTACATCACTTGCAC	4b position
4[461]-3[447]	GTTAGCCGGAACGAGGCTTTGAGGACCAACCTAAAACT	Core staples
12[20]-11[6]	AGCCATCAAAAATAATTATTATTACAAAAGGAATTACC	Core staples
0[468]-8[469]	CTGGAAGTTGAGAGGTCATTTTTGGTCTTTAAAATATTCATAGCGTC	Core staples
0[118]-4[116]	AAGGCCGGAGACAGTCCGAAATCCGCTGGTCTTCACCGCCTGGGG	Core staples
4[178]-15[188]	CCTGACATTTAAAAGATAACATCGCCGCTACAACCACCACACCCGCC	Core staples
11[238]-9[253]	ATTGCGAATGGATTGTTTGGATTATAGCGGAAAATACCAAG	Core staples
14[209]-8[189]	ACAACTCGCACTAATGGAAGGTTATCTAAAATAGAAG	Core staples

0[27]-8[28]	CTATCAGGGATAAACGATGCTGATAGACTTTCGGATAACGCTTTCAG	Core staples
3[259]-6[259]	GTTAATTTCATGTTTTCAAATATATCAAAGAACGGCGTTAA	Core staples
9[353]-4[357]	GACTTTTTCATCGCCTCCCTCAGAGCCCCTCAGCCAGCATTGGCCT	Core staples
1[504]-6[493]	ATAATGAAAACAGGTCAGGATTAGAGAGCTTAATTAATG	Core staples
11[175]-9[190]	GTGTTTCTAAACCCTCGTTAGAATCTTAATGCACTTGCCTG	Core staples
7[399]-0[385]	TCGCCCACAGAAGGATTAGGATGTTAATGCGCAAATGGTCAATAA	Core staples
6[6]-14[7]	CAAATGACAGTTGATAATCATTTTTTCATTAAATATTAAATG	Core staples
0[496]-4[494]	ATGTTTTAAATATGCAGCTTAGAGTACCTTAACCAGACCGGAAAG	Core staples
6[69]-14[70]	CCAACCACGCGTCAGCGTGGCGGGGTTTACGGCTCCCTGCGG	Core staples
14[69]-12[84]	CTGGTTGCTCGGGCGCGGTTGCGGTATGAGCCCCGCGGGC	Core staples
15[504]-14[21]	ATGAGTAACAACCCGTCGGATTCTCCGTGGGAGGCTTT	Core staples
0[132]-6[115]	TTCAAAAAAATCAACCGTTGCAGCAAGCGGTCCAGGCAAAATCTTT	Core staples
1[17]-0[497]	AATCTCATTGCCTGAGAGTCTGGCTGTAGCTCAAC	Core staples
6[132]-14[133]	GGCGACATTGAACGTGGACTAAATCGTTGGGGTCGAAGGGAA	Core staples
11[259]-4[273]	ATAAAGCCAAATTACAAATAAATACCGACCGTCCGATTT	Core staples
0[69]-6[52]	AAATTAATTCGTCTTCAAAAAAAGCCGCACAGGCAACGCGGTCAGT	Core staples
0[55]-4[53]	AGGGTAGCTATTTTTGTCCGGCAGGCCTTTACATCGACATAAGCG	Core staples
4[482]-3[468]	GAAAGACCAAAGCGTAATTGCTCCTTTTGATATCTAATTC	8a position
3[280]-11[279]	GTCAAAAAGAAATTTCCACGTTTTTATTTTAAATCGG	5b position
9[227]-4[231]	GATTTCAATTAAAACAAAATTAATTAGGAAACATTGCTTCCTTAGA	Core staples
9[380]-0[371]	CGGTGGTAACCATCGATAGGAGGTTGCCCTCAGAGTAACAAGCTATAT	Core staples
0[433]-4[431]	TGCGAACGAGTAGATTGAAACAAACACTAAACTACGAAGGCACTA	Core staples
11[343]-9[352]	CATTACCCAGCAGGAAATTATTCATAGGGAAGTCA	Core staples
4[367]-15[377]	GATTGACAGCAGCACGTTTTCATTCAACCGACCAGCGCCAAAGACAA	Core staples
4[20]-3[6]	CGATCATATGTACCCCGAAAAGATTAGCAAACTCCAAC	Core staples
15[441]-14[462]	ACGAACGAGTAGTAAATTGGGCTTGAGATGGAGAGGCT	Core staples
7[273]-0[259]	GCGGGAGGCGTGTGATAAATAAGCGAGAATAAAGCCTCAGAGCAT	Core staples
0[342]-8[343]	ATCAATTCAGTACTGGTAATAAGACCAGAACACCGGAACAATCAAAA	Core staples
11[416]-0[406]	GAATAAATCTCGGAACGAACCCTCACAAGCGCTAGTTTGACCATTAG	Core staples
8[503]-7[20]	AGAGGGGGAAACAGTTCAATTTAAATTGTAAACGTTAGC	Core staples
15[350]-11[352]	AATTCATATGGTTTATTGAGGGTAAAGGTTTGGGAATTAGAGCAT	Biotin position
8[188]-7[209]	AACTCAAATTTGACGCTCACAGTTGAAAGGAATTGAGAT	Core staples
0[447]-6[430]	GTTGATTTGTATCATGCGAAAGAGGCAAAAGAATAGTACAACTTTT	Core staples
11[353]-0[343]	TAGCAGTAGCGGCCGCCGAGCCGCCTTTTAACAGCTGAAAAGGTGGC	Core staples
12[335]-11[321]	CCTATGTTAGCAAACGTTAATATCCCGGGTATTAAACT	Core staples
9[128]-0[119]	GAATTGATCTTCGCGTCCGGAGGCGGCTGCCCGCCCTTATGGGTGAGA	Core staples
15[35]-11[37]	GCGGATTGACCGTAATAACCGTTCGGCCTGGCACCGCTTCTGGCC	Biotin position
9[101]-4[105]	TAATATACGAGGAGTGAGCTAACTCATCGGGAACAACGCGCAGGGT	Core staples
9[164]-4[168]	TTTGTAATATCAACGCTCATGGAAATTATTTACTAAAAGGTCTGAC	Core staples
0[370]-4[368]	TTTCATTTGGGGCGCGGGGGTCACATGGCTAAAGCGCAGTCTGAC	Core staples
11[427]-9[442]	GAACAATTTCTGTTTCCAGACGTTACGCCTGTGCTTGCTTT	Core staples
15[476]-11[478]	CAACTTTAATCATTGTATACCATAAAACGAAAGATTCATCAGAAT	Biotin position
4[493]-15[503]	AGGAAGCGGAGAGCAAGGCTTTTTGGCTCATTGAATTACCTTATGCG	Core staples
15[378]-14[399]	AATTTCAGGGATAGCAAGCCCAATAGGAACCGTCCACC	Core staples
4[419]-3[405]	TCATGAGTAATGCCAACACTCATCTTTGACCCCCGGGTAA	7a position
0[244]-4[242]	GTACCAAAAACATTATTAAATGCCTACCTTAGAGTCAATAGTTTT	Core staples
4[209]-3[195]	TAGCATCACCTTGCTGAAGAGATAGTTAATGCGCGAGA	Core staples
6[492]-11[489]	ACCAAATGCTTTTAATAGTAAAATGTTTTAGCGAGACACTATATACAT	Core staples
9[443]-0[434]	CGAGGCCGCGAATAATAATTACAGAGAGGCCGCGGAGATTCCCAATTC	Core staples
8[405]-15[412]	TGACAACAGGCTCCAAAAGGAGCTAGTTAGCCATGTACC	Core staples
15[189]-14[210]	GCTGCCCGAACGTTATTAATTTTAAAAGTTTGGATTCG	Core staples
4[104]-3[90]	GGTTTTTGATTGCCTTGCCCCAGCAGGCGAAAGGCGGGCA	2a position
3[385]-6[385]	TATTATTCTGACCTGCCTATTTCGGTATAAACATAGCGGGG	Core staples
4[304]-15[314]	TTAAGTTACCTCATCATAGCAAGAAACAACAAAGTAATTCTGTCCAG	Core staples
11[101]-0[91]	GGGGAGTTGAGAATCGGCACCTGTCGTGGTTCAAATCACCATCAATA	Core staples
14[146]-8[126]	GAGAAAGGAGGTGCCCTCACCCAAATCAAGTTATTGT	Core staples
3[70]-6[70]	AACGGAACGTGACCAGAGCACATCCCGTCGCTGCAAGAATG	Core staples
4[41]-3[27]	TAAATTTGTTGTGTAGTGATGAAGGGTAAAGTTGAGCAGT	1a position
6[366]-11[363]	ACCACGCCACCCATTAGCGTTTGCCATCGTAGCGCCGTAATCAAGGCC	Core staples
4[115]-15[125]	CGCCGGGGATGAGCCATAGCTGTCGGGTTACCAGCAAATCGTTAACG	Core staples
6[429]-11[426]	GCGGTGAGGCTTAACAGCTTGATACCGATGTATCGACGTTGAAGAAAG	Core staples
0[258]-6[241]	AAAGCTACGCAAGATTAATCATAGGTCTGAGAGATGATGCAATTTT	Core staples
7[84]-0[70]	GCCTGGGGTGCAGCAGCAACCGGCAGCCTAACCGTTCTAGCTGAT	Core staples
15[224]-11[226]	TTATCATTTTGCGGAATATTCCATCCTGAAGGGTTAGAACCTCAG	Biotin position
3[406]-11[405]	AATACGGAAGTTAGCATCCAAAAAAAAGGAAGTTTCA	7b position
4[335]-3[321]	AATGAAATAGCAATAGCAGCCATATACAGAGAGAATAG	Core staples
11[112]-9[127]	CCAGCATCTGTGAGTGTCACTGCGCCAGATGCTTCCTGTGT	Core staples
3[91]-11[90]	ACAGCTCTTTTCTTAATGGATCCCCGGGTCATTCACG	2b position
4[52]-15[62]	GATACGGAAGGCCTCTGGGTAACGCGCATCGTGGGATAGGTCACGTT	Core staples
7[147]-0[133]	CCATTGCAAGGGCGAAAAACCGCCCGAGAAATGTGTAGGTAAAGA	Core staples
4[146]-3[132]	TGGAGTCCACTATTAAATGCGTATTGCCCTGAGAGAAG	Core staples

7[210]-0[196]	GAAACAAATACAATATCTGGTCTGCCACGGAAGCCTTTATTTCAA	Core staples
9[254]-0[245]	TTATGCAGTTTAACGTCAGTCGTCGCATTACCTATCCAATAATCGGTT	Core staples
9[317]-0[308]	TATACTCCCAAGTACCGCAAAAATAACTACAATAATATCATCCAATAA	Core staples
3[154]-11[153]	AATATTCGTAAGACACGAGCAAATTAACCTAGAACGG	3b position
12[83]-11[69]	CGTCGCACTCAATCCGCCCAGCCAGTGTTGGGAAGGTT	Core staples
4[230]-3[216]	ATCCTTGGCTGAGATTTAACCTCCGGCTTAGGGATTAGAT	4a position
14[83]-8[63]	ACTGTTGGGAGGTGTACCATCCCACGCAACCACCAGT	Core staples
8[90]-15[97]	ATAAAGTGTCACCGAGCTCGAATGCCGGTGCAACATCCC	Core staples
11[280]-9[289]	CTGTCTGTAGAATTTATCAACAATACTAATGCCAT	Core staples
12[209]-11[195]	TTTACATTTGAGGATTTAGCGGGAGTTATAATCAGTGT	Core staples
11[448]-4[462]	ATATTCATTATAATCTTGAATCATAAGGGAACTTATCGC	Core staples
11[38]-0[28]	ATTCTTACGCCAAGGGATTGAGAGATTGCCGTAGAGATCTACAAAGG	Core staples
4[241]-15[251]	TCCTGTAAAATGAATTTGCTTTGTTATCATCACAAAGAAACCACCAG	Core staples
9[38]-4[42]	GGCGGTGCCAACTCACCGGAAACAATGAATTTGAGCTCTCCAAACT	Core staples
11[290]-0[280]	CTTAAGCAAGCGAGCCTAACCAACGAGTCAGAAAAGAATTAGCAAAA	Core staples
11[479]-0[469]	GCAGCATAACCTATAGTCAAAATCAGCGGATGACTAAAGTACGGTGT	Core staples
8[125]-7[146]	TATCCGCTGCGTTGCGCTTGGCCCACTACGTGAACCAAG	Core staples
11[469]-9[478]	TCAACTTTGAGAAAATCTACGTTAAGTCAGGAACC	Core staples
14[258]-12[273]	TAGGCGGACCTTAATTGAGAATCGCCATATTTTGACCAAT	Core staples
3[196]-6[196]	AAAATCTAAAGCGAGCCAGCAGCAATGCAACAGAGTTGGCA	Core staples
11[364]-9[379]	GGAAACAGCCATGAATTATCACCGTGCGACATCGGCATTTT	Core staples
6[114]-11[111]	CCAGCATTAATTCACAATTCCACACAACCATGGTCTCCTCACTTTCTG	Core staples
0[195]-6[178]	CGCAAGGCACCGCCATACTGATAGCCCTAAAACAGGCGGTCAAAAT	Core staples
7[336]-0[322]	GAGCCACCCAGAAAAGTAAGCAAGAATTGTACTAATAGTAGTAGC	Core staples
14[384]-12[399]	CTCATGGCACAGAACCGCCACCCTCAGAACCGAAACTTTC	Core staples
14[447]-12[462]	CACCAAAGTCAAAGCTGCTCATTCAGTGAATAAATTTAGG	Core staples
0[153]-8[154]	GCCTGAGTTACACCAGCAGAAGAGATTCACCACAGGAAACAGAACAA	Core staples
6[240]-11[237]	TAATCATTTAACAGGCGAATTATTCATTCGCCTGAATACAGTAAAGAA	Core staples
8[440]-7[461]	ATTTCTTAGCAGGGAGTTACAGATGAACGGTGTACAGGA	Core staples
6[303]-11[300]	TCCTAGTTGCTAGGTATTCTAAGAACGCGCGCCCAGAGAACATCATTC	Core staples
15[63]-14[84]	GGAATGGGTAAAGGTTTCTTTGCTCGTCATACCGGGTC	Core staples
8[314]-7[335]	GCTTATCCTTTTGCACCCAGTTACCAGAAGGAAACCGCA	Core staples
9[479]-4[483]	AAAAAGACTGGATTGAATCCCCCTCATAAATCAAGAAGCAAAGCCC	Core staples
0[384]-6[367]	CCTGTTTGTGCCCGAAGTTCCAGTAAGCGTCATAGTGCCTTGAGCC	Core staples
8[342]-15[349]	TCACCGGAACTTTGCCTTTAGCGGTAAATATCAATAGAA	Core staples
15[413]-11[415]	GTAACACTGAGTTTCACAGACATGTCGTCTATGGGATTTTGCTGA	Biotin position
4[430]-15[440]	AAGAACGGCTTTTTCGTTTATCAAGCATTCCGTCACCAGTACAAACT	Core staples
7[462]-0[448]	ATCGTCATCCCCGAACTGACCATAAATTGTTCATTCCATATAACA	Core staples
15[126]-14[147]	GCCGAAAGGAGCGGGCGCTAGGGCGCTGGCATGGTGGC	Core staples
8[27]-15[34]	AGGTGGAGAAGGGGGATGTGCTGCCAGTTTGAACAAACG	Core staples
11[385]-4[399]	TCAGGAGGTTCATAGGTGTACTCCTCAAGAGACTCCATT	Core staples
4[167]-3[153]	CTGAAAGTTTGAATTAAAAATACCGAACGAACGGACAGAC	3a position
8[251]-7[272]	TCGCGCAGAATTTCATTTAATAAACACCGGAATCATATT	Core staples
14[398]-8[378]	CTCAGAGATAGCCCACGTGCCGTCGAGAGGGTTCATA	Core staples
14[461]-8[441]	TGCCCTGCATCAAGCGACCAGGCGCATAGGCTGGTGA	Core staples
0[181]-4[179]	TTTTAGAACCCTCATAGAGGTGATCGCCATGGCTATTAGTCTAAC	Core staples
11[406]-9[415]	GCGGAGTAAACACGATCTAAAGTTTGCCCTCACTT	Core staples
15[98]-11[100]	TTACACTGGTGTGTTCTGCAGCCCAGCGCGTGCTGCGGCCAGCCG	Biotin position
9[191]-0[182]	AGTATCCGAGGCCACCGAGCTGGCCATCGTCTGGTATTAAATAAAAAT	Core staples
0[405]-8[406]	ATACATTTCCCCAGCGATTATACGCAGCGAAGCATAACCGCCGACAA	Core staples
3[322]-6[322]	CAAGAAACAATCAAGCCCAATAATAAACCCACAGATAGCCG	Core staples
12[398]-11[384]	AATAGTACCGCCACCCTCCGACTTGGTCACCAATGAAC	Core staples
1a-4[41]-3[27]	TAAATTTGTTGTGTAGTGATGAAGGGTAAAGTTGAGCAGTAAGATCTACATA	DNA-PAINT docking at 1a position
2a-4[104]-3[90]	GGTTTTTGATTGCCTTGCCCCAGCAGGCGAAAGGCGGGCAAAGATCTACATA	DNA-PAINT docking at 2a position
3b-3[154]-11[153]	GATCTACATAAAAATATTCGTAAGACACGAGCAAATTAACCTAGAACGG	DNA-PAINT docking at 3b position
4a-4[230]-3[216]	ATCCTTGGCTGAGATTTAACCTCCGGCTTAGGGATTAGATAAGATCTACATA	DNA-PAINT docking at 4a position
5a-4[293]-3[279]	TCCAAATAATGAAAGACGGGAGAATTAACTGACTTTTAACAAGATCTACATA	DNA-PAINT docking at 5a position
6a-4[356]-3[342]	TGATATTAGAATGGTTTGATGATACAGGAGTGTTCTCATTAAGATCTACATA	DNA-PAINT docking at 6a position
7a-4[419]-3[405]	TCATGAGTAATGCCAACACTCATCTTTGACCCCCGGGTAAAAGATCTACATA	DNA-PAINT docking at 7a position
8a-4[482]-3[468]	GAAAGACCAAAGCGTAATTGCTCCTTTTGATATCTAATTCAAGATCTACATA	DNA-PAINT docking at 8a position
Docking-mid-10nt-3Aspacer	GGATAAGGAAGGTGGGCAGGAAAGATCTACATAAAACGTTTGTTAGGGATTGGGTG	DNA-PAINT docking for tension study
biotin-4T-15[35]-11[37]	/5Biosg/TTTTGCGGATTGACCGTAATAACCGTTCGGCCTGGCACCGCTTCTGGCC	Biotinylated strands
biotin-4T-15[98]-11[100]	/5Biosg/TTTTTTACACTGGTGTGTTCTGCAGCCCAGCGCGTGCTGCGGCCAGCCG	Biotinylated strands
biotin-4T-15[161]-11[163]	/5Biosg/TTTTGGTCACGCTGCGCGTAGGGCGCGTGCTTTAGGAGGCCGATTAAGA	Biotinylated strands
biotin-4T-15[224]-11[226]	/5Biosg/TTTTTTATCATTTTGCGGAATATTCCATCCTGAAGGGTTAGAACCTCAG	Biotinylated strands
biotin-4T-15[287]-11[289]	/5Biosg/TTTTTACCGACAAAAGGTATGTTCAGGATAAGTAATTTACGAGCATTTC	Biotinylated strands
biotin-4T-15[350]-11[352]	/5Biosg/TTTTAATTCATATGGTTTATTGAGGGTAAAGGTTTGGGAATTAGAGCAT	Biotinylated strands
biotin-4T-15[413]-11[415]	/5Biosg/TTTTGTAACACTGAGTTTCACAGACATGTCGTCTATGGGATTTTGCTGA	Biotinylated strands
biotin-4T-15[476]-11[478]	/5Biosg/TTTTCAACTTTAATCATTGTATACCATAAAACGAAAGATTCATCAGAAT	Biotinylated strands

200nt ssDNA spring 2-3[406]-11[405]	CCTGCCCACCTTCCTTATCCTTT

Name	Sequence	Tension Configuration
x-extension to spring 2 r Cy5-b Cy3-h-extension to spring 1	GGATAAGGAAGGTGGGCAGGTTTCCCAGTTGAGCGCTTGCTAGGG CCCACCGCTCGGCTCAACTGGG /Cy5/CCCTAGCAAGCCGCTGCTACGG /Cy3/CCGTAGCAGCGCGAGCGGTGGGTTTCGTTTGTTAGGGATTGGGTG	Single-axial y-axis
Cy3-h Cy5-b r x-extension to spring 2 and spring 1	/Cy3/CCGTAGCAGCGCGAGCGGTGGG /Cy5/CCCTAGCAAGCCGCTGCTACGG CCCACCGCTCGGCTCAACTGGG GGATAAGGAAGGTGGGCAGGTTTCCCAGTTGAGCGCTTGCTAGGG TTTCGTTTGTTAGGGATTGGGTG	Single-axial x-axis
x-extension to spring 2 and spring 3 r Cy5-b Cy3-h-extension to spring 1	GGATAAGGAAGGTGGGCAGGTTTCCCAGTTGAGCGCTTGCTAGGGT TTATAATGTGAGAAAGAAAAGG CCCACCGCTCGGCTCAACTGGG /Cy5/CCCTAGCAAGCCGCTGCTACGG /Cy3/CCGTAGCAGCGCGAGCGGTGGGTTTCGTTTGTTAGGGATTGGGTG	Three-way tension 1
Cy3-h-extension to spring 3 Cy5-b r x-extension to spring 2 and spring 1	/Cy3/CCGTAGCAGCGCGAGCGGTGGGTTTATAATGTGAGAAAGAAAAGG /Cy5/CCCTAGCAAGCCGCTGCTACGG CCCACCGCTCGGCTCAACTGGG GGATAAGGAAGGTGGGCAGGTTTCCCAGTTGAGCGCTTGCTAGGGTT TCGTTTGTTAGGGATTGGGTG	Three-way tension 2
Cy3-h r-extension to spring 4 x-extension to spring 2 and spring 3 Cy5-b-extension to spring 1	/Cy3/CCGTAGCAGCGCGAGCGGTGGG AAGAGTAAGGATGAAAGGAATTTCCCACCGCTCGGCTCAACTGGG GGATAAGGAAGGTGGGCAGGTTTCCCAGTTGAGCGCTTGCTA GGGTTTATAATGTGAGAAAGAAAAGG /Cy5/CCCTAGCAAGCCGCTGCTACGGTTTCGTTTGTTAGGGATTGGGTG	Four-way tension

Table S2 HJ strands for various tension forces configuration. Set of DNA strands to form HJ for specific tension forces configuration. We mixed each set consisting of 4 strands in equimolar final concentration of 200 nM in a final 1× TAE 12.5 mM Mg^{2+}.

Tension	Strands	Final Concentration
0 pN	p8064 scaffold	20 nM
	Core staples (excluding biotin and 3a positions)	200 nM/strand
	Biotinylated staples	200 nM/strand
	4[167]-3[153]-200nt ssDNA spring 1	500 nM/strand
	1× TAE 12.5 mM $MgCl_2$ buffer	1×
2 pN	p8064 scaffold	20 nM
	Core staples (excluding biotin, 3a, and 7b positions)	200 nM/strand
	Biotinylated staples	200 nM/strand
	4[167]-3[153]-200nt ssDNA spring 1	500 nM/strand
	200nt ssDNA spring 2-3[406]-11[405]	500 nM/strand
	1× TAE 12.5 mM $MgCl_2$ buffer	1×
3 pN	p8064 scaffold	20 nM
	Core staples (excluding biotin, 3a, and 7b positions)	200 nM/strand
	Biotinylated staples	200 nM/strand
	4[167]-3[153]-200nt ssDNA spring 1	500 nM/strand
	117nt ssDNA spring 2-3[406]-11[405]	500 nM/strand
	1× TAE 12.5 mM $MgCl_2$ buffer	1×
6 pN	p8064 scaffold	20 nM
	Core staples (excluding biotin, 3a, and 7b positions)	200 nM/strand
	Biotinylated staples	200 nM/strand
	4[167]-3[153]-120nt ssDNA spring 1	500 nM/strand
	117nt ssDNA spring 2-3[406]-11[405]	500 nM/strand
	1× TAE 12.5 mM $MgCl_2$ buffer	1×
9 pN	p8064 scaffold	20 nM
	Core staples (excluding biotin, 3a, and 7b positions)	200 nM/strand
	Biotinylated staples	200 nM/strand
	4[167]-3[153]-100nt ssDNA spring 1	500 nM/strand
	117nt ssDNA spring 2-3[406]-11[405]	500 nM/strand
	1× TAE 12.5 mM $MgCl_2$ buffer	1×
Three-way	p8064 scaffold	20 nM
	Core staples (excluding biotin, 1a, 3a, and 7b positions)	200 nM/strand
	Biotinylated staples	200 nM/strand
	4[167]-3[153]-200nt ssDNA spring 1	500 nM/strand
	117nt ssDNA spring 2-3[406]-11[405]	500 nM/strand
	4[41]-3[27]-200nt ssDNA spring 3	500 nM/strand
	1× TAE 12.5 mM $MgCl_2$ buffer	1×
Four-way	p8064 scaffold	20 nM
	Core staples (excluding biotin, 1a, 3a, 5b, and 7b positions)	200 nM/strand
	Biotinylated staples	200 nM/strand
	4[167]-3[153]-200nt ssDNA spring 1	500 nM/strand
	117nt ssDNA spring 2-3[406]-11[405]	500 nM/strand
	4[41]-3[27]-200nt ssDNA spring 3	500 nM/strand
	117nt ssDNA spring 4-3[280]-11[279]	500 nM/strand
	1× TAE 12.5 mM $MgCl_2$ buffer	1×

Table S3 MAESTRO mixing concentrations across different tension conditions.

Strands	**Final Concentration**
p8064 scaffold	20 nM
Core staples (staples at biotin, 1a, 2a, 3b, 4a, 5a, 6a, 7a, and 8a positions should be excluded)	200 nM/strand
Biotinylated staples	200 nM/strand
DNA-PAINT dockings	1000 nM/strand
1× TAE 12.5 mM $MgCl_2$ buffer	1×

Table S4 MAESTRO mixing concentrations for DNA-PAINT assay.

Parameters	**Values**
$k_{\text{off}}(0)$	0.07 s^{-1}
Δx_{off}	0.32 nm
$k_{\text{on}}(0)$	2.63 $\mu M^{-1}s^{-1}$
$\frac{1}{a}$	-0.115 $pN^{-1}nm$
b	0.84 nm

Table S5 Fitted values of kinetics parameters for short oligos under tension.

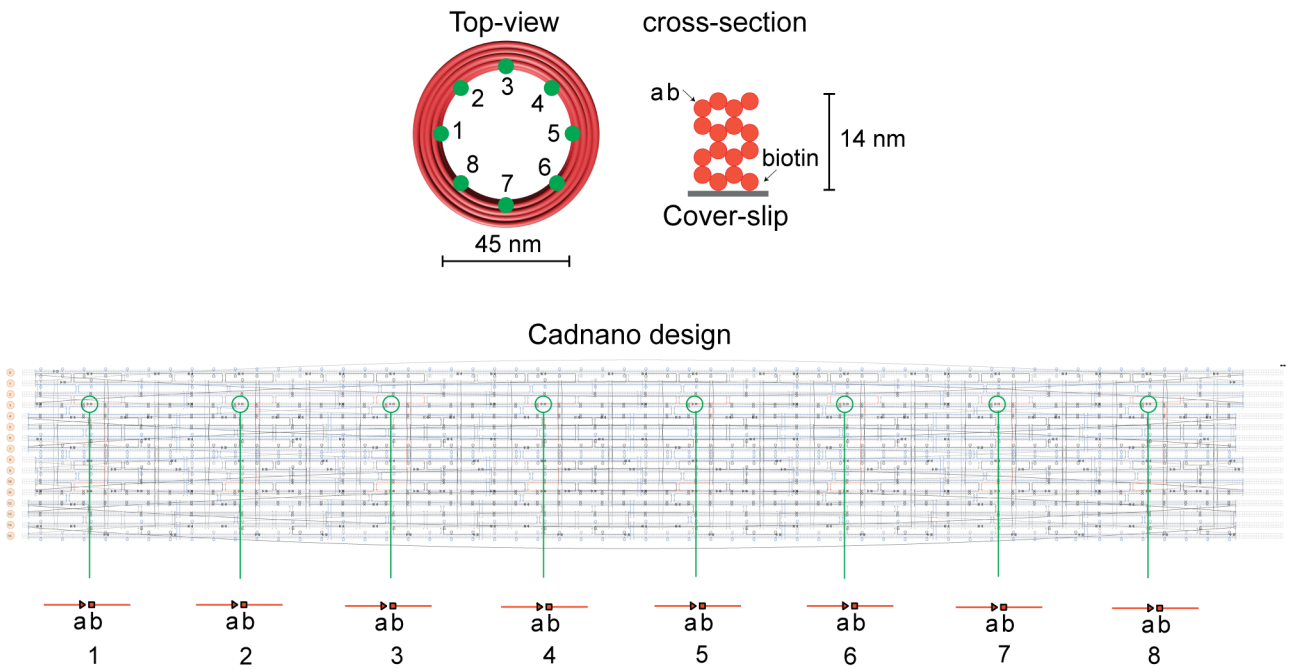

Fig. S1 MAESTRO schematics (top) and cadnano design (bottom) showing the position of points 1a,b to 8a,b corresponding to some strands in Table S1

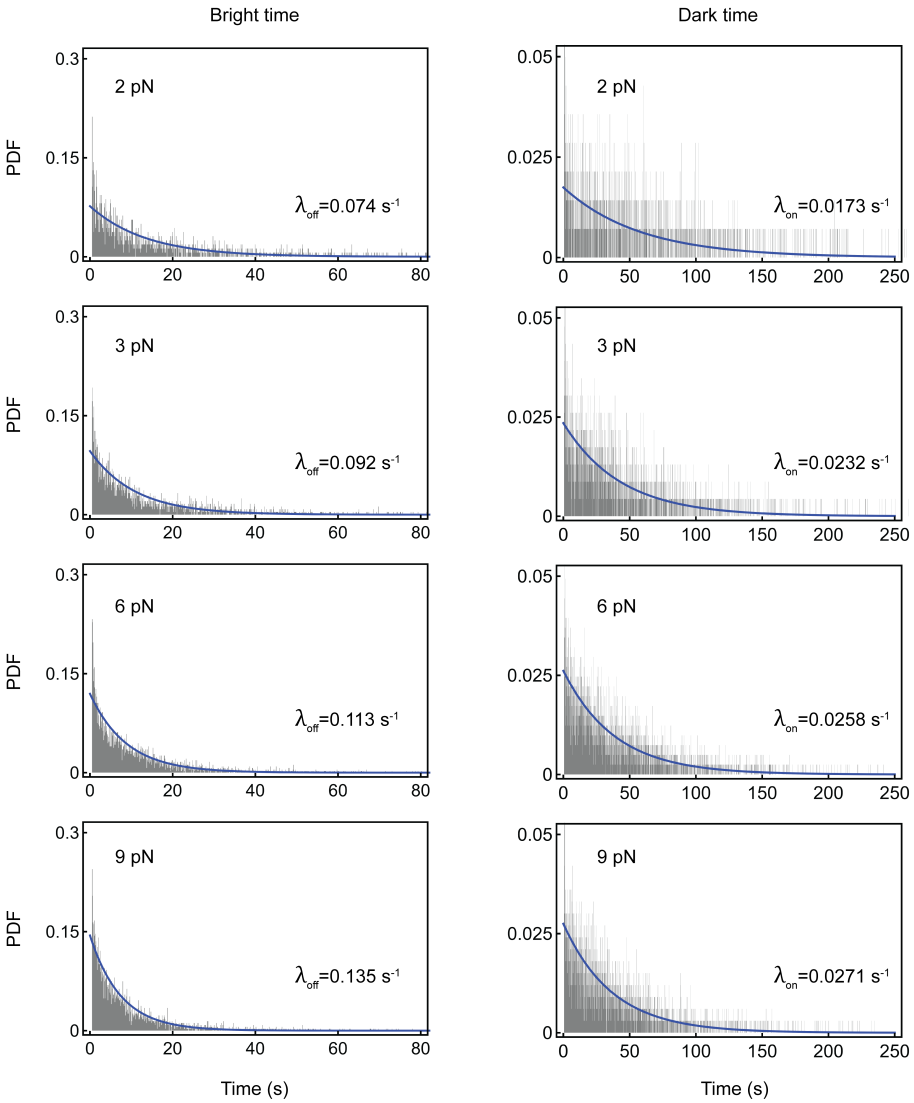

Fig. S2 Histogram plots of bright (left) and dark times (right) of short oligos under various tension forces, using a bin width of 100 ms—equal to the camera exposure time—along with exponential fit curves (blue).

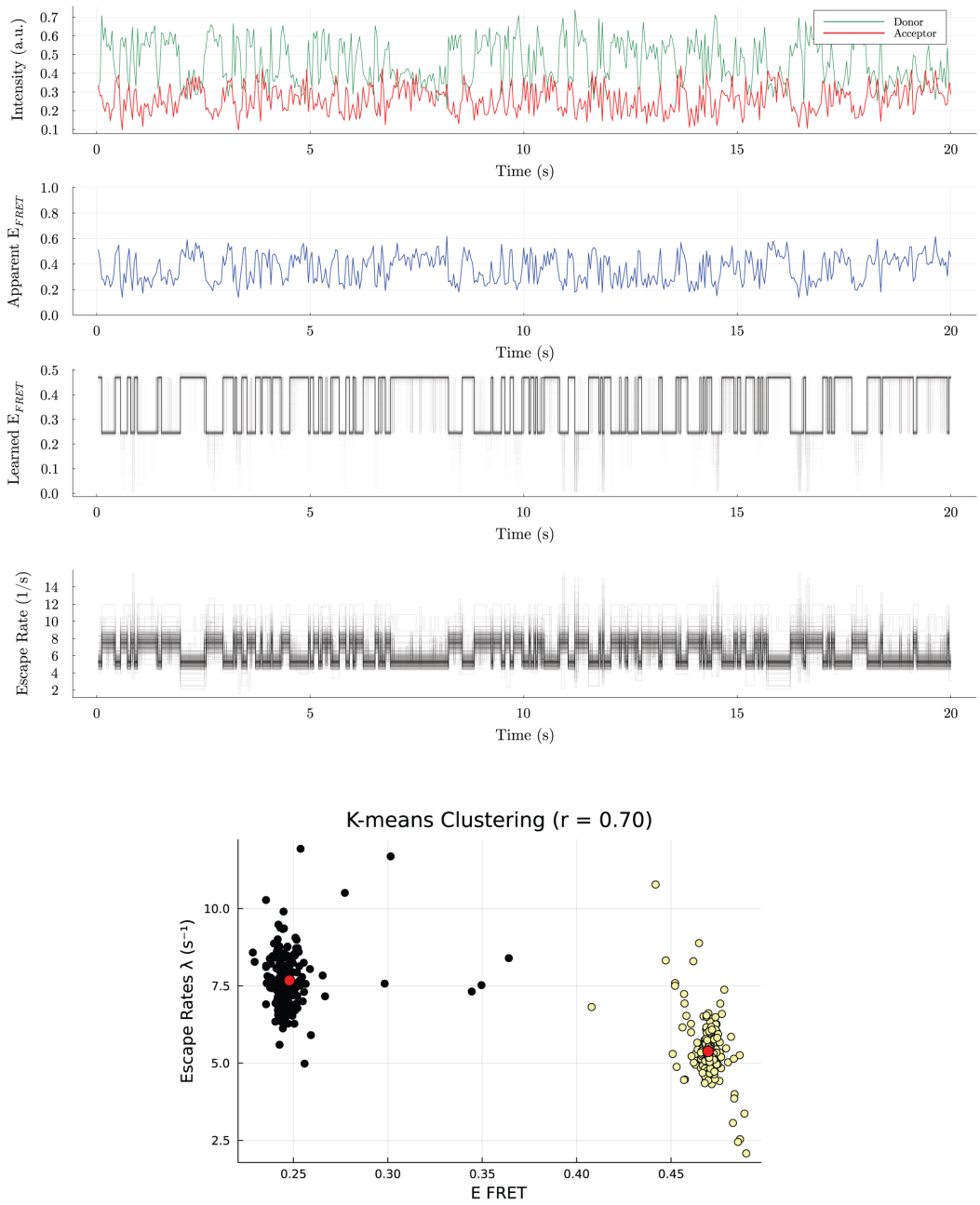

Fig. S3 **An example of a smFRET trajectory showing donor's and acceptor's emissions at 0 pN (1st row), the apparent FRET efficiency (2nd row), the learned FRET efficiency (3rd row), the learned escape rates (4th row), and the escape rates k-means clustering performed on MCMC samples generated by BNP-FRET to extract the mean escape rate λ values of Iso-I and Iso-II used to calculate the ratio $r = \lambda_{\text{Iso-I}}/\lambda_{\text{Iso-II}}$ where red dots show the mean values for each cluster colored in black and yellow (5th row)**

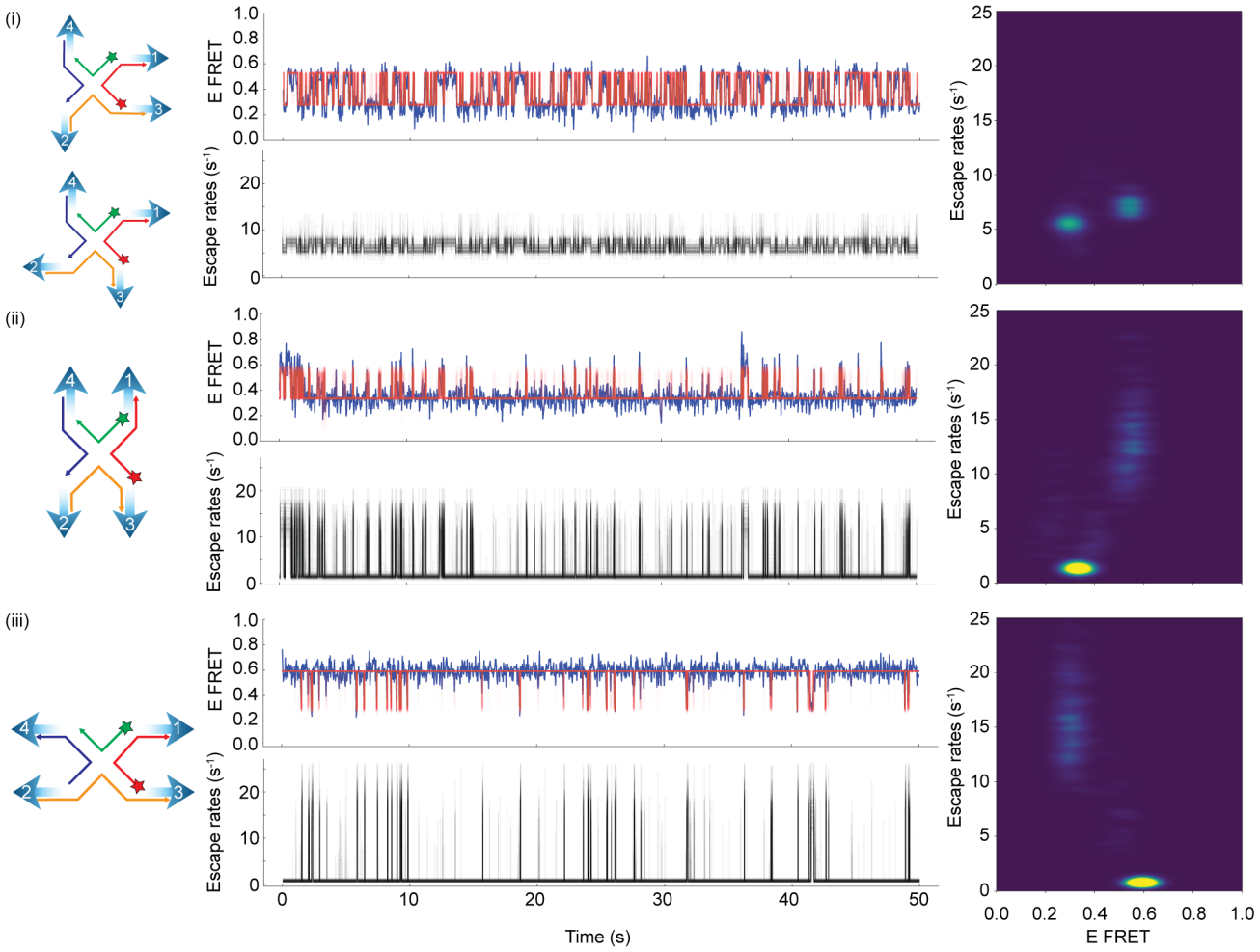

Fig. S4 **Additional examples of smFRET traces from the four-way tension force configuration, illustrating the proposed direction of tension forces on the molecules, along with their corresponding trace and escape rate heatmaps. These examples include traces that switch between Iso-I and Iso-II (i), remain stuck at Iso-II (ii), and remain stuck at Iso-I (iii).**

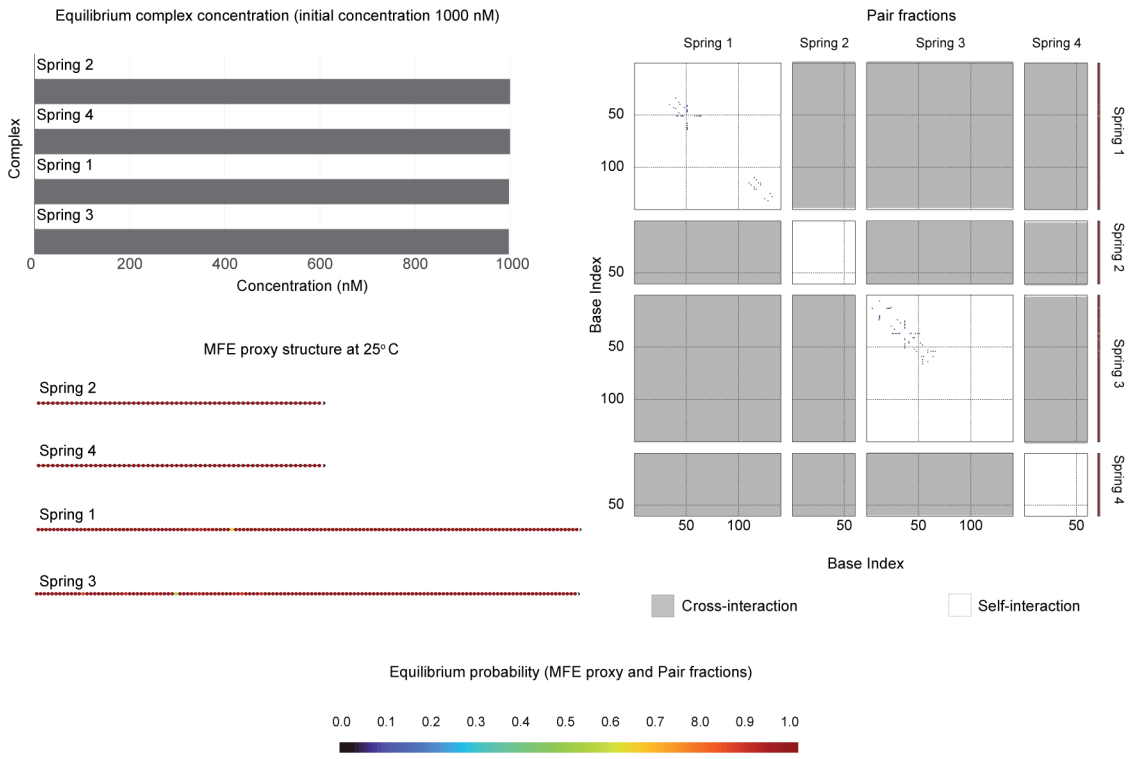

Fig. S5 **NUPACK analysis of the ssDNA springs at 25°C showing the equilibrium complex concentrations, pair fractions, and minimum free energy (MFE) proxy structures. The results indicate that all ssDNA springs exhibit negligible self- and cross-interactions, as evidenced by the MFE proxy structures and pair interaction profiles.**

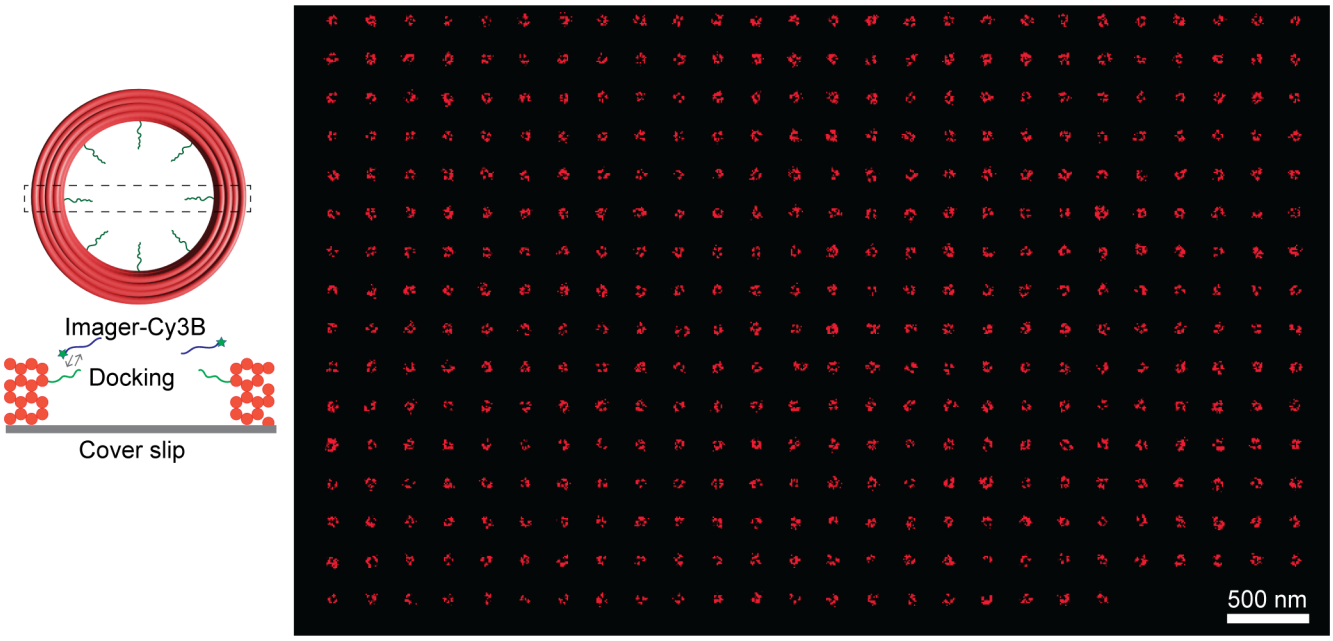

Fig. S6 **MAESTRO DNA-PAINT schematics illustrating the arrangement of docking strands and the organization of all selected molecules in an array.**